



HAL
open science

Lagrangian modelling of large deformation induced by progressive failure of sensitive clays with elastoviscoplasticity

Xue Zhang, Daichao Sheng, Scott W Sloan, Jeremy Bleyer

► **To cite this version:**

Xue Zhang, Daichao Sheng, Scott W Sloan, Jeremy Bleyer. Lagrangian modelling of large deformation induced by progressive failure of sensitive clays with elastoviscoplasticity. *International Journal for Numerical Methods in Engineering*, 2017, 112 (8), pp.963-989. 10.1002/nme.5539 . hal-01485340

HAL Id: hal-01485340

<https://enpc.hal.science/hal-01485340>

Submitted on 8 Mar 2017

HAL is a multi-disciplinary open access archive for the deposit and dissemination of scientific research documents, whether they are published or not. The documents may come from teaching and research institutions in France or abroad, or from public or private research centers.

L'archive ouverte pluridisciplinaire **HAL**, est destinée au dépôt et à la diffusion de documents scientifiques de niveau recherche, publiés ou non, émanant des établissements d'enseignement et de recherche français ou étrangers, des laboratoires publics ou privés.

1 Lagrangian modelling of large deformation induced by progressive failure of
2 sensitive clays with elastoviscoplasticity

3
4 (Dated: Nov 30, 2016)

5 Xue Zhang^{1*}, Daichao Sheng¹, Scott W Sloan¹, Jeremy Bleyer²

6 1. ARC Centre of Excellence for Geotechnical Science and Engineering,
7 University of Newcastle, University Drive, Callaghan, NSW, 2308,
8 Australia

9 2. Université Paris-Est, Laboratoire Navier, (Ecole des Ponts ParisTech-
10 IFSTTAR-CNRS UMR 8205), 6-8 av. Blaise Pascal, 77420 Champs-Sur-
11 Marne, France

12 Abstract

13 This paper presents a Lagrangian formulation of elastoviscoplasticity, based on the Particle
14 Finite Element Method, for progressive failure analysis of sensitive clays. The sensitive clay
15 is represented by an elastoviscoplastic model which is a mixture of the Bingham model, for
16 describing rheological behaviour, and the Tresca model with strain softening for capturing
17 the progressive failure behaviour. The finite element formulation for the incremental
18 elastoviscoplastic analysis is reformulated, through the application of the Hellinger-Reissner
19 variational theorem, as an equivalent optimization program that can be solved efficiently
20 using modern algorithms such as the interior-point method. The recast formulation is then
21 incorporated into the framework of the Particle Finite Element Method for investigating
22 progressive failure problems related to sensitive clays, such as the collapse of a sensitive clay
23 column and the retrogressive failure of a slope in sensitive clays, where extremely large
24 deformation occurs.

25 **Keywords:** Sensitive clays; Progressive failure; Elastoviscoplasticity; Strain softening;
26 PFEM; Mathematical programming; SOCP

27 _____
28 * xue.zhang@uon.edu.au

29 1. Introduction

30 Sensitive clay is characterized by a decrease in its shear strength when experiencing plastic
31 deformation. A highly sensitive clay may possess sensitivity, defined as a ratio of the
32 undisturbed shear strength and the remoulded shear strength, of the order of magnitude of a
33 hundred. For example, the reported values of the sensitivity of the clay involved in the 1893
34 Verdalen landslide and the 2012 Byneset landslide are 300 and 120, respectively [1]. Due to
35 the strong strain-softening behaviour, geostructures built on a layer of sensitive clay often fail
36 in a progressive manner. Moreover, unexpectedly catastrophic failure of the geostructure
37 might also be induced by a small perturbation. Typical examples are the multiple
38 retrogressive slides and spreads in sensitive clays observed in Canada and Scandinavia [2],
39 which occurred suddenly, covered large areas (more than 1 hectare) and were caused by an
40 initially small slope failure.

41

42 Reliable prediction of the progressive failure behaviour of sensitive clays is of critical
43 importance. It can provide guidelines for relevant engineering practice, for example
44 construction on sensitive clays, and also assist in minimizing the degree of destruction caused
45 by potential geohazards (such as the fore-mentioned large landslides). Although numerical
46 simulation is a powerful tool for analyzing complex geotechnical problems, robust modelling
47 of the large deformations induced by progressive failure in sensitive clays is still a formidable
48 task. Indeed, a major challenge is the complex behaviour that is typically exhibited by
49 sensitive clays. An undisturbed sensitive clay usually behaves like a solid body, but may
50 change to be a semi-liquid material after being remolded [1]. The transformation between
51 these two states is caused by strain softening. Suitable constitutive models must be capable of
52 describing the rheological behaviour of a sensitive clay, since this is crucial for estimating the
53 run-out distance of landslides [3-5] as well as capturing the strain-softening behaviour that

54 contributes to the phenomenon of progressive failure [2, 6, 7]. Sensitive clays typically
55 undergo extremely large deformation along localized shear zones due to strain-softening.
56 This feature can cause severe mesh distortion when the traditional finite element method is
57 adopted and result in computational difficulties. Additionally, the free-surface evolution
58 induced by extreme deformation also challenges the use of the traditional FEM because of its
59 use of a fixed mesh topology. Recently, some alternative numerical approaches have been
60 proposed for modelling the progressive failure of sensitive clays involving large deformation.
61 Wang *et. al* [8] studied retrogressive and progressive slope failure in sensitive clays using the
62 material point method. Dey *et. al* [9-11] analyzed the spread in sensitive clay slopes due to
63 progressive failure by implementing a strain-softening model into the ABAQUS Coupled
64 Eulerian Lagrangian approach. Although these procedures reproduced the pronounced
65 progressive failure behaviour of sensitive clays, it is notable that classical rate-independent
66 models were utilised. However, ignoring the rheology of sensitive clays may lead to the
67 inaccurate predictions. Analytical approaches, such as shear band propagation approaches
68 [12-16], have also been used to study the progressive failure process in catastrophic
69 landslides in nature. Recent developments in the shear band propagation approach for
70 analyzing catastrophic and progressive failure are summarized in [17].

71

72 This paper provides an alternative Lagrangian computational approach for the analysis of
73 progressive failure of sensitive clays involving extremely large deformation. An advanced
74 elastoviscoplastic constitutive relationship, which is a combination of the Bingham model
75 and the Tresca model with strain softening, is adopted for describing their complex behaviour.
76 To solve the resulting elastoviscoplastic problem with strain softening, a generalized
77 incremental Hellinger-Reissner variational theorem [18] is proposed which recasts the
78 associated governing equations into an equivalent min-max program. After finite element

79 discretisation, the resulting problem can be converted into a standard second-order cone
80 programming problem which may be solved efficiently using modern optimization
81 algorithms (for example, the primal-dual interior point method [19]). Typical advantages of
82 such a solution strategy include the possibility of analyzing the existence, uniqueness,
83 sensitivity and stability of the solution [20], the natural treatment of the singularities in the
84 Mohr-Coulomb and Drucker-Prager yield criteria [21-23], the straightforward extension from
85 single-surface plasticity to multi-surface plasticity [21], and the straightforward
86 implementation of contact between deformable and rigid bodies [24, 25]. The proposed
87 solution algorithm is incorporated into the framework of the Particle Finite Element Method
88 (PFEM) [26-28] for handling large deformation. The PFEM is a novel continuum approach
89 suitable for simulating problems involving both solid-like and fluid-like behaviour [27, 29,
90 30]. It makes use of particles to represent the material, as in meshfree particle methods, but
91 solves the governing equations via a standard finite element procedure. Consequently, the
92 PFEM inherits both the solid mathematical foundation of the traditional FEM as well as the
93 capability of meshfree particle methods for handling extremely large deformation and free-
94 surface evolution.

95

96 The paper is organized as follows. Section 2 presents the governing equations for dynamic
97 analysis of an elastoviscoplastic problem. An incremental mixed variational principle is then
98 proposed in Section 3 for recasting the governing equations into a min-max problem. Finite
99 element discretisation is performed in Section 4, and the Particle Finite Element Method is
100 described briefly in Section 5. Numerical examples are given in Section 6, before conclusions
101 are drawn in Section 7.

102

103 2. Governing equations for elastoviscoplasticity

104 Consider a medium with volume Ω and surface $\Gamma = \Gamma_u \cup \Gamma_t$, where Γ_u and Γ_t are the
 105 kinematic and traction boundaries, respectively. The partition of the surface obeys the
 106 constraint $\Gamma_u \cap \Gamma_t = \emptyset$ where \emptyset is a null set. The momentum conservation equation, the
 107 kinematic equations for displacement gradients, and the corresponding boundary conditions
 108 read

$$109 \quad \nabla^T \boldsymbol{\sigma} + \mathbf{b} = \rho \ddot{\mathbf{u}} \quad \text{in } \Omega \quad (1)$$

$$110 \quad \boldsymbol{\varepsilon} = \nabla^T \mathbf{u} \quad \text{in } \Omega \quad (2)$$

$$111 \quad \mathbf{u} = \bar{\mathbf{u}} \quad \text{on } \Gamma_u \quad (3)$$

$$112 \quad \mathbf{N}^T \boldsymbol{\sigma} = \bar{\mathbf{t}} \quad \text{on } \Gamma_t \quad (4)$$

113 where $\boldsymbol{\sigma}$ and $\boldsymbol{\varepsilon}$ are the Cauchy stress and the strain, \mathbf{b} is the body force, \mathbf{u} is the
 114 displacement, $\bar{\mathbf{u}}$ and $\bar{\mathbf{t}}$ are the prescribed displacements and external tractions, \mathbf{N} consists
 115 of components of the outward normal to the boundary Γ_t , and ∇ is the usual linear operator
 116 taking the form of

$$117 \quad \nabla^T = \begin{bmatrix} \frac{\partial}{\partial x} & 0 & 0 & \frac{\partial}{\partial y} \\ 0 & \frac{\partial}{\partial y} & 0 & \frac{\partial}{\partial x} \end{bmatrix} \quad (5)$$

118 in a plane-strain case. A superposed dot represents differentiation with respect to time.

119

120 Assuming the material is elastoviscoplastic, the total strain rate $\dot{\boldsymbol{\varepsilon}}$ can then be split into an
 121 elastic strain rate $\dot{\boldsymbol{\varepsilon}}^e$ and a viscoplastic strain rate $\dot{\boldsymbol{\varepsilon}}^{vp}$

$$122 \quad \dot{\boldsymbol{\varepsilon}} = \dot{\boldsymbol{\varepsilon}}^e + \dot{\boldsymbol{\varepsilon}}^{vp} \quad (6)$$

123 The elastic strain rate is determined through Hook's law as

$$124 \quad \dot{\boldsymbol{\varepsilon}}^e = \mathbb{C} \dot{\boldsymbol{\sigma}} \quad (7)$$

125 where \mathbb{C} is the elastic compliance matrix. The material is elastic if the stress state is inside
 126 the yield domain, namely

$$127 \quad F(\boldsymbol{\sigma}) < 0 \Rightarrow \dot{\boldsymbol{\epsilon}}^{vp} = \mathbf{0} \quad (8)$$

128 where F is the yield function. In contrast, stress states satisfying $F(\boldsymbol{\sigma}) \geq 0$ lead to a
 129 viscoplastic strain rate. The classical Bingham model is utilized in this paper for describing
 130 the rheological properties of the sensitive clay. Despite its simple form, it performs well for
 131 approximating the plastic flow behaviour of these soils, especially Canadian clays [5]. The
 132 total stress thus is rewritten as

$$133 \quad \boldsymbol{\sigma} = \boldsymbol{\tau} + \eta \dot{\boldsymbol{\epsilon}}^{vp} \quad (9)$$

134 where η is the viscosity coefficient, $\boldsymbol{\tau}$ is the stress lying on the boundary of F so that
 135 $F(\boldsymbol{\tau}) = 0$, and the quantity $\boldsymbol{\sigma} - \boldsymbol{\tau}$ is called the overstress. The viscoplastic strain rate is also
 136 normal to the yield surface at $\boldsymbol{\tau}$:

$$137 \quad \dot{\boldsymbol{\epsilon}}^{vp} = \dot{\lambda} \nabla_{\boldsymbol{\tau}} F(\boldsymbol{\tau}) \quad (10)$$

138 where $\dot{\lambda}$ is the rate of the non-negative plastic multiplier and $\nabla_{\boldsymbol{\tau}}$ is the gradient operator. It is
 139 clear that the above elastoviscoplastic model reduces to the classical elastoplastic model in
 140 the limiting case of $\eta = 0$.

141

142 Laboratory tests show that the undrained shear strength of a sensitive clay decreases with
 143 increasing plastic shear strain. For materials exhibiting softening/hardening behaviour, the
 144 yield criterion function is expressed by $F(\boldsymbol{\tau}, \boldsymbol{\kappa}) = 0$, where $\boldsymbol{\kappa}$ is a set of hardening/softening
 145 variables which relate to the viscoplastic strain in the form of

$$146 \quad \boldsymbol{\kappa} = H(\boldsymbol{\epsilon}^{vp}) \quad (11)$$

147 Specifically, for the Tresca yield criterion, we have

148
$$F(\boldsymbol{\sigma}, \kappa) = \sqrt{(\sigma_{xx} - \sigma_{yy})^2 + 4\sigma_{xy}^2} - 2c_u(\kappa) \quad (12)$$

149 where cohesion softening is adopted to capture the basic post-failure behaviour. Following
 150 [31, 32], strain-softening is accounted for by reducing the cohesion c_u using a bilinear
 151 function (Figure 1) of the equivalent deviatoric plastic strain, $\kappa = \int \dot{\kappa} dt$, where
 152 $\dot{\kappa} = \sqrt{0.5 \dot{\epsilon}_{ij}^{vp} \dot{\epsilon}_{ij}^{vp}}$ and $\dot{\epsilon}_{ij}^{vp}$ is the rate of deviatoric viscoplastic strain tensor given by

153
$$\dot{\epsilon}_{ij}^{vp} = \dot{\epsilon}_{ij}^{vp} - \frac{1}{3} \dot{\epsilon}_{kk}^{vp} \delta_{ij} \quad (13)$$

154 in which δ_{ij} is the Kronecker delta.

155

156 3. Variational principle

157 3.1 Hellinger-Reissner variational principle

158 The Hellinger-Reissner (HR) variational principle is of a mixed kind. Unlike the principle of
 159 minimum potential energy, in which displacements are considered as the only master field,
 160 the Hellinger-Reissner variational principle treats both the displacements and the stresses as
 161 the master fields [18].

162

163 For an elastostatic boundary-value problem, the Hellinger-Reissner functional [18] may be
 164 expressed as

165
$$\Pi(\boldsymbol{\sigma}, \mathbf{u}) = \int_{\Omega} \left(-\frac{1}{2} \boldsymbol{\sigma}^T \mathbf{C} \boldsymbol{\sigma} + \boldsymbol{\sigma}^T \mathbf{S}^T \mathbf{u} \right) d\Omega - \int_{\Omega} \mathbf{b}^T \mathbf{u} d\Omega - \int_{\Gamma_t} \bar{\mathbf{t}}^T \mathbf{u} d\Gamma \quad (14)$$

166 The stationary value for the Hellinger-Reissner functional cannot be shown to be an
 167 extremum. Instead, the point obtained by $\delta \Pi(\boldsymbol{\sigma}, \mathbf{u}) = 0$ is a saddle point and, consequently,
 168 the problem becomes one of a min-max optimisation:

169
$$\min_{\mathbf{u}} \max_{\boldsymbol{\sigma}} \int_{\Omega} \left(-\frac{1}{2} \boldsymbol{\sigma}^T \mathbb{C} \boldsymbol{\sigma} + \boldsymbol{\sigma}^T \mathbf{S}^T \mathbf{u} \right) d\Omega - \int_{\Omega} \mathbf{b}^T \mathbf{u} d\Omega - \int_{\Gamma_t} \bar{\mathbf{t}}^T \mathbf{u} d\Gamma \quad (15)$$

170 where the internal work is maximised with respect to the stresses and the total potential
171 energy is minimised with respect to the displacements.

172

173 3.2 Generalised Hellinger-Reissner variational principle

174 A generalised Hellinger-Reissner variational principle is proposed for incremental analysis of
175 elastoviscoplasticity. The governing equations summarised in section 2 are first discretized in
176 time using the standard θ -method. Details of the time discretisation, as well as the resulting
177 incremental equations, are documented in Appendix A.

178

179 We present here the generalized incremental Hellinger-Reissner variational principle for
180 incremental elasto-viscoplastic analysis. As for elastostatics, the principle is expressed in the
181 form of a min-max program:

$$\begin{aligned}
 \min_{\Delta \mathbf{u}} \max_{(\boldsymbol{\sigma}, \boldsymbol{\tau}, \mathbf{r})_{n+1}} & -\frac{1}{2} \int_{\Omega} \Delta \boldsymbol{\sigma}^T \mathbb{C} \Delta \boldsymbol{\sigma} d\Omega + \int_{\Omega} \boldsymbol{\sigma}_{n+1}^T \nabla^T (\Delta \mathbf{u}) d\Omega + \int_{\Omega} \frac{1-\theta_1}{\theta_1} \boldsymbol{\sigma}_n^T \nabla^T (\Delta \mathbf{u}) d\Omega \\
 & -\frac{1}{2} \int_{\Omega} \mathbf{r}_{n+1}^T \frac{\Delta t^2}{\tilde{\rho}} \mathbf{r}_{n+1} d\Omega + \int_{\Omega} \mathbf{r}_{n+1}^T \Delta \mathbf{u} d\Omega \\
 182 & -\frac{1}{2} \int_{\Omega} (\Delta \boldsymbol{\sigma} - \Delta \boldsymbol{\tau})^T \frac{\theta_3 \Delta t}{\eta} (\Delta \boldsymbol{\sigma} - \Delta \boldsymbol{\tau}) d\Omega - \int_{\Omega} \Delta \boldsymbol{\sigma}^T \frac{\Delta t}{\eta} (\boldsymbol{\sigma}_n - \boldsymbol{\tau}_n) d\Omega \\
 & + \int_{\Omega} (\boldsymbol{\sigma}_n - \boldsymbol{\tau}_n)^T \frac{\Delta t}{\eta} \Delta \boldsymbol{\tau} d\Omega - \int_{\Omega} \tilde{\mathbf{b}}^T \Delta \mathbf{u} d\Omega - \int_{\Gamma_t} \tilde{\mathbf{t}}^T \Delta \mathbf{u} d\Gamma \\
 \text{subject to} & F(\boldsymbol{\tau}_{n+1}) \leq 0
 \end{aligned} \quad (16)$$

183 where \mathbf{r} is a set of variables that can be interpreted as dynamic forces. To illustrate the
184 equivalence between the program (16) and the incremental form of the governing equations
185 presented in Appendix A, the Karush-Kuhn-Tucker (KKT) optimality conditions associated
186 with (16) are now derived. Following [23, 33], the inequality constraint is first converted into
187 an equality by adding a positively-restricted variable s_{n+1} . Then, the inequality on s_{n+1} is

188 represented by introducing a penalty term in the objective function:

$$\begin{aligned}
\min_{\Delta \mathbf{u}} \max_{(\boldsymbol{\sigma}, \boldsymbol{\tau}, \mathbf{r})_{n+1}} & -\frac{1}{2} \int_{\Omega} \Delta \boldsymbol{\sigma}^T \mathbb{C} \Delta \boldsymbol{\sigma} d\Omega + \int_{\Omega} \boldsymbol{\sigma}_{n+1}^T \nabla^T (\Delta \mathbf{u}) d\Omega + \int_{\Omega} \frac{1-\theta_1}{\theta_1} \boldsymbol{\sigma}_n^T \nabla^T (\Delta \mathbf{u}) d\Omega \\
& -\frac{1}{2} \int_{\Omega} \mathbf{r}_{n+1}^T \frac{\Delta t^2}{\tilde{\rho}} \mathbf{r}_{n+1} d\Omega + \int_{\Omega} \mathbf{r}_{n+1}^T \Delta \mathbf{u} d\Omega \\
189 & -\frac{1}{2} \int_{\Omega} (\Delta \boldsymbol{\sigma} - \Delta \boldsymbol{\tau})^T \frac{\theta_3 \Delta t}{\eta} (\Delta \boldsymbol{\sigma} - \Delta \boldsymbol{\tau}) d\Omega - \int_{\Omega} \Delta \boldsymbol{\sigma}^T \frac{\Delta t}{\eta} (\boldsymbol{\sigma}_n - \boldsymbol{\tau}_n) d\Omega \\
& + \int_{\Omega} (\boldsymbol{\sigma}_n - \boldsymbol{\tau}_n)^T \frac{\Delta t}{\eta} \Delta \boldsymbol{\tau} d\Omega - \int_{\Omega} \tilde{\mathbf{b}}^T \Delta \mathbf{u} d\Omega - \int_{\Gamma_t} \tilde{\mathbf{t}}^T \Delta \mathbf{u} d\Gamma + \int_{\Omega} \mu \ln s_{n+1} d\Omega \\
\text{subject to} & F(\boldsymbol{\tau}_{n+1}) + s_{n+1} = 0
\end{aligned} \tag{17}$$

190 where μ is a sufficiently small positive constant. The penalty term $\mu \ln s_{n+1}$ in the objective
191 function imposes the non-negativity requirement on s_{n+1} naturally, and is known as a
192 logarithmic barrier function. The Lagrangian associated with program (17) is

$$\begin{aligned}
& \mathcal{L}(\Delta \mathbf{u}, \boldsymbol{\sigma}_{n+1}, \boldsymbol{\tau}_{n+1}, \mathbf{r}_{n+1}, \Delta \lambda, s_{n+1}) \\
& = -\frac{1}{2} \int_{\Omega} \Delta \boldsymbol{\sigma}^T \mathbb{C} \Delta \boldsymbol{\sigma} d\Omega + \int_{\Omega} \boldsymbol{\sigma}_{n+1}^T \nabla^T (\Delta \mathbf{u}) d\Omega + \int_{\Omega} \frac{1-\theta_1}{\theta_1} \boldsymbol{\sigma}_n^T \nabla^T (\Delta \mathbf{u}) d\Omega \\
193 & -\frac{1}{2} \int_{\Omega} \mathbf{r}_{n+1}^T \frac{\Delta t^2}{\tilde{\rho}} \mathbf{r}_{n+1} d\Omega + \int_{\Omega} \mathbf{r}_{n+1}^T \Delta \mathbf{u} d\Omega - \frac{1}{2} \int_{\Omega} (\Delta \boldsymbol{\sigma} - \Delta \boldsymbol{\tau})^T \frac{\theta_3 \Delta t}{\eta} (\Delta \boldsymbol{\sigma} - \Delta \boldsymbol{\tau}) d\Omega \\
& - \int_{\Omega} \Delta \boldsymbol{\sigma}^T \frac{\Delta t}{\eta} (\boldsymbol{\sigma}_n - \boldsymbol{\tau}_n) d\Omega + \int_{\Omega} (\boldsymbol{\sigma}_n - \boldsymbol{\tau}_n)^T \frac{\Delta t}{\eta} \Delta \boldsymbol{\tau} d\Omega - \int_{\Omega} \tilde{\mathbf{b}}^T \Delta \mathbf{u} d\Omega - \int_{\Gamma_t} \tilde{\mathbf{t}}^T \Delta \mathbf{u} d\Gamma \\
& + \int_{\Omega} \mu \ln s_{n+1} d\Omega - \int_{\Omega} \Delta \lambda (F(\boldsymbol{\tau}_{n+1}) + s_{n+1}) d\Omega
\end{aligned} \tag{18}$$

194 The KKT optimality conditions are found by differentiating the above Lagrangian with
195 respect to the optimisation variables, namely:

$$\frac{\partial \mathcal{L}}{\partial \Delta \mathbf{u}} = \begin{cases} \nabla^T \boldsymbol{\sigma}_{n+1} + \frac{1-\theta_1}{\theta_1} \nabla^T \boldsymbol{\sigma}_n + \mathbf{r}_{n+1} - \tilde{\mathbf{b}} = \mathbf{0} & \text{in } \Omega \\ \mathbf{N}^T (\boldsymbol{\sigma}_{n+1} + \frac{1-\theta_1}{\theta_1} \boldsymbol{\sigma}_n) = \tilde{\mathbf{t}} & \text{on } \Gamma_t \end{cases} \tag{19}$$

$$\frac{\partial \mathcal{L}}{\partial \boldsymbol{\sigma}_{n+1}} = \nabla^T (\Delta \mathbf{u}) - \mathbb{C} \Delta \boldsymbol{\sigma} - \frac{\theta_3 \Delta t}{\eta} (\Delta \boldsymbol{\sigma} - \Delta \boldsymbol{\tau}) - \frac{\Delta t}{\eta} (\boldsymbol{\sigma}_n - \boldsymbol{\tau}_n) = \mathbf{0} \quad \text{in } \Omega \tag{20}$$

$$198 \quad \frac{\partial \mathcal{L}}{\partial \boldsymbol{\tau}_{n+1}} = \frac{\theta_3 \Delta t}{\eta} (\Delta \boldsymbol{\sigma} - \Delta \boldsymbol{\tau}) + \frac{\Delta t}{\eta} (\boldsymbol{\sigma}_n - \boldsymbol{\tau}_n) - \Delta \lambda \nabla_G F(\boldsymbol{\tau}_{n+1}) = \mathbf{0} \quad \text{in } \Omega \quad (21)$$

$$199 \quad \frac{\partial \mathcal{L}}{\partial \mathbf{r}_{n+1}} = \frac{\Delta t^2}{\tilde{\rho}} \mathbf{r}_{n+1} - \Delta \mathbf{u} = \mathbf{0} \quad \text{in } \Omega \quad (22)$$

$$200 \quad \frac{\partial \mathcal{L}}{\partial \Delta \lambda} = F(\boldsymbol{\tau}_{n+1}) + s_{n+1} = 0 \quad \text{in } \Omega \quad (23)$$

$$201 \quad \frac{\partial \mathcal{L}}{\partial s_{n+1}} = \mu s_{n+1}^{-1} - \Delta \lambda = 0 \Rightarrow \mu = s_{n+1} \Delta \lambda \quad \text{in } \Omega \quad (24)$$

202 It is apparent that the KKT conditions (19)-(22) are equivalent to the corresponding
 203 incremental equations presented in Appendix A. The last two conditions recover the yield
 204 condition and the complementarity condition shown in (50) when $\mu \rightarrow 0^+$, given that the
 205 penalty multiplier $\Delta \lambda \geq 0$, and $s_{n+1} > 0$. The essential boundary condition (40) is assumed to
 206 hold *a priori*, and thus is not reflected in the KKT conditions. From condition (22) we can
 207 also see that the newly introduced variables \mathbf{r} are dynamic forces.

208

209 3.3 Material hardening/softening

210 The variational principle (16) can also be extended to handle more complex models involving
 211 hardening/softening yield surfaces following [34]. More specifically, the min-max program
 212 considering material hardening/softening is expressed as:

$$\begin{aligned}
& \min_{\Delta \mathbf{u}} \max_{(\boldsymbol{\sigma}, \boldsymbol{\tau}, \mathbf{r})_{n+1}} -\frac{1}{2} \int_{\Omega} \Delta \boldsymbol{\sigma}^T \mathbb{C} \Delta \boldsymbol{\sigma} d\Omega + \int_{\Omega} \boldsymbol{\sigma}_{n+1}^T \nabla^T (\Delta \mathbf{u}) d\Omega + \int_{\Omega} \frac{1-\theta_1}{\theta_1} \boldsymbol{\sigma}_n^T \nabla^T (\Delta \mathbf{u}) d\Omega \\
& -\frac{1}{2} \int_{\Omega} \mathbf{r}_{n+1}^T \frac{\Delta t^2}{\tilde{\rho}} \mathbf{r}_{n+1} d\Omega + \int_{\Omega} \mathbf{r}_{n+1}^T \Delta \mathbf{u} d\Omega \\
213 \quad & -\frac{1}{2} \int_{\Omega} (\Delta \boldsymbol{\sigma} - \Delta \boldsymbol{\tau})^T \frac{\theta_3 \Delta t}{\eta} (\Delta \boldsymbol{\sigma} - \Delta \boldsymbol{\tau}) d\Omega - \int_{\Omega} \Delta \boldsymbol{\sigma}^T \frac{\Delta t}{\eta} (\boldsymbol{\sigma}_n - \boldsymbol{\tau}_n) d\Omega \quad (25) \\
& + \int_{\Omega} (\boldsymbol{\sigma}_n - \boldsymbol{\tau}_n)^T \frac{\Delta t}{\eta} \Delta \boldsymbol{\tau} d\Omega - \frac{1}{2} \int_{\Omega} \mathcal{H}_t^{-1} \Delta \kappa^2 d\Omega - \int_{\Omega} \tilde{\mathbf{b}}^T \Delta \mathbf{u} d\Omega - \int_{\Gamma_t} \tilde{\mathbf{t}}^T \Delta \mathbf{u} d\Gamma \\
& \text{subject to } F(\boldsymbol{\tau}_{n+1}, \kappa_{n+1}) \leq 0
\end{aligned}$$

214 The underlined term is the newly introduced one with \mathcal{H}_t being a new constitutive modulus
215 associated with hardening/softening. The according KKT condition related to the variable κ
216 is

$$217 \quad \frac{\partial \mathcal{L}}{\partial \kappa_{n+1}} = -\mathcal{H}_t^{-1} \Delta \kappa - \Delta \lambda \nabla_{\kappa} F(\boldsymbol{\tau}_{n+1}, \kappa_{n+1}) = 0 \Rightarrow \Delta \kappa = -\Delta \lambda \mathcal{H}_t \nabla_{\kappa} F(\boldsymbol{\tau}_{n+1}, \kappa_{n+1}) \quad (26)$$

218 which is the hardening/softening law, i.e. the evolution law, for the variable κ . The
219 constitutive modulus, \mathcal{H}_t , can be derived by first expanding Eq. (11) using a Taylor series

$$220 \quad \kappa_{n+1} = \kappa_n + \frac{dH(\boldsymbol{\varepsilon}_n^{\text{vp}})}{d\boldsymbol{\varepsilon}^{\text{vp}}} \Delta \boldsymbol{\varepsilon}^{\text{vp}} \Rightarrow \Delta \kappa = \frac{dH(\boldsymbol{\varepsilon}_n^{\text{vp}})}{d\boldsymbol{\varepsilon}^{\text{vp}}} \Delta \boldsymbol{\varepsilon}^{\text{vp}} \quad (27)$$

221 Since Eq. (26) cannot be brought to be equal to the actual hardening/softening law (27) using
222 a constant modulus, we therefore use the following tangent modulus as in [34]

$$223 \quad \mathcal{H}_t = -\frac{dH(\boldsymbol{\varepsilon}_n^{\text{vp}})}{d\boldsymbol{\varepsilon}^{\text{vp}}} \frac{\nabla_{\boldsymbol{\tau}} F(\boldsymbol{\tau}_n, \kappa_n)}{\nabla_{\kappa} F(\boldsymbol{\tau}_n, \kappa_n)} \quad (28)$$

224 which is updated at the beginning of each time step. Such a treatment of material
225 hardening/softening behaviour in mathematical programming has been used successfully for
226 approximating the hardening/softening behaviour in the Cam clay model [34].

227

228 4. Finite element formulation

229 The min-max program (25) can now be discretized using finite elements. For the sake of
 230 convenience, an intermediate variable $\boldsymbol{\sigma}^e = \boldsymbol{\sigma} - \boldsymbol{\tau}$ (overstress) is introduced, which enables
 231 the optimization problem (25) to be expressed as

$$\begin{aligned}
 \min_{\Delta \mathbf{u}} \max_{(\boldsymbol{\sigma}, \boldsymbol{\tau}, \boldsymbol{\sigma}^e, \mathbf{r})_{n+1}} & -\frac{1}{2} \int_{\Omega} \Delta \boldsymbol{\sigma}^T \mathbb{C} \Delta \boldsymbol{\sigma} d\Omega + \int_{\Omega} \boldsymbol{\sigma}_{n+1}^T \nabla^T (\Delta \mathbf{u}) d\Omega + \int_{\Omega} \frac{1-\theta_1}{\theta_1} \boldsymbol{\sigma}_n^T \nabla^T (\Delta \mathbf{u}) d\Omega \\
 & -\frac{1}{2} \int_{\Omega} \mathbf{r}_{n+1}^T \frac{\Delta t^2}{\tilde{\rho}} \mathbf{r}_{n+1} d\Omega + \int_{\Omega} \mathbf{r}_{n+1}^T \Delta \mathbf{u} d\Omega \\
 232 & -\frac{1}{2} \int_{\Omega} \Delta \boldsymbol{\sigma}^{eT} \frac{\theta_3 \Delta t}{\eta} \Delta \boldsymbol{\sigma}^e d\Omega - \int_{\Omega} \Delta \boldsymbol{\sigma}^{eT} \frac{\Delta t}{\eta} \boldsymbol{\sigma}_n^e d\Omega \\
 & -\frac{1}{2} \int_{\Omega} \mathcal{H}_i^{-1} \Delta \kappa^2 d\Omega - \int_{\Omega} \tilde{\mathbf{b}}^T \Delta \mathbf{u} d\Omega - \int_{\Gamma_i} \tilde{\mathbf{t}}^T \Delta \mathbf{u} d\Gamma \\
 \text{subject to} & \Delta \boldsymbol{\sigma}^e = \Delta \boldsymbol{\sigma} - \Delta \boldsymbol{\tau} \\
 & F(\boldsymbol{\tau}_{n+1}, \kappa_{n+1}) \leq 0
 \end{aligned} \tag{29}$$

233 Using standard finite element notations, we have

$$\begin{aligned}
 234 & \boldsymbol{\sigma}(\mathbf{x}) \approx \mathbf{N}_{\boldsymbol{\sigma}} \hat{\boldsymbol{\sigma}}, \quad \boldsymbol{\sigma}^e(\mathbf{x}) \approx \mathbf{N}_{\boldsymbol{\sigma}^e} \hat{\boldsymbol{\sigma}}^e, \quad \boldsymbol{\tau}(\mathbf{x}) \approx \mathbf{N}_{\boldsymbol{\tau}} \hat{\boldsymbol{\tau}}, \\
 & \mathbf{r}(\mathbf{x}) \approx \mathbf{N}_{\mathbf{r}} \hat{\mathbf{r}}, \quad \mathbf{u}(\mathbf{x}) \approx \mathbf{N}_{\mathbf{u}} \hat{\mathbf{u}}, \quad \nabla^T \mathbf{u} \approx \mathbf{B}_{\mathbf{u}} \hat{\mathbf{u}}, \\
 & \kappa(\mathbf{x}) \approx \mathbf{N}_{\kappa} \hat{\kappa}
 \end{aligned} \tag{30}$$

235 where $\hat{\boldsymbol{\sigma}}$, $\hat{\boldsymbol{\sigma}}^e$, $\hat{\boldsymbol{\tau}}$, $\hat{\mathbf{r}}$, $\hat{\mathbf{u}}$, and $\hat{\kappa}$ are vectors containing the values of the corresponding field
 236 variables at interpolation points, \mathbf{N} is a matrix consisting of shape functions, and $\mathbf{B}_{\mathbf{u}} = \nabla^T \mathbf{N}_{\mathbf{u}}$
 237 . The mixed finite element shown in Figure 2 is adopted in this study, where the distribution
 238 of the interpolation points for the different variables is depicted. Substituting the above
 239 equations into the program (29) leads to

$$\begin{aligned}
& \min_{\Delta \hat{\mathbf{u}}} \max_{(\hat{\boldsymbol{\sigma}}, \hat{\boldsymbol{\tau}}, \hat{\boldsymbol{\sigma}}^e, \hat{\mathbf{r}}, \hat{\mathbf{k}})_{n+1}} -\frac{1}{2} \Delta \hat{\boldsymbol{\sigma}}^T \mathbf{C} \Delta \hat{\boldsymbol{\sigma}} + \Delta \hat{\mathbf{u}}^T \mathbf{B}^T \hat{\boldsymbol{\sigma}}_{n+1} + \Delta \hat{\mathbf{u}}^T \frac{1-\theta_1}{\theta_1} \mathbf{B}^T \hat{\boldsymbol{\sigma}}_n \\
& -\frac{1}{2} \hat{\mathbf{r}}_{n+1}^T \mathbf{D} \hat{\mathbf{r}}_{n+1} + \Delta \hat{\mathbf{u}}^T \mathbf{A}^T \hat{\mathbf{r}}_{n+1} - \frac{1}{2} \Delta \hat{\boldsymbol{\sigma}}^{eT} \mathbf{M} \Delta \hat{\boldsymbol{\sigma}}^e \\
& -\Delta \hat{\boldsymbol{\sigma}}^{eT} \mathbf{f}^c - \frac{1}{2} \Delta \hat{\mathbf{k}}^T \mathbf{H} \Delta \hat{\mathbf{k}} - \Delta \hat{\mathbf{u}}^T \mathbf{f}^e
\end{aligned} \tag{31}$$

$$\text{subject to } \Delta \hat{\boldsymbol{\sigma}}^e = \Delta \hat{\boldsymbol{\sigma}} - \Delta \hat{\boldsymbol{\tau}}$$

$$F_j(\hat{\boldsymbol{\tau}}_{n+1}, \hat{\mathbf{k}}_{n+1}) \leq 0, \quad j=1, 2, \dots, N_G$$

241 where

$$\begin{aligned}
\mathbf{C} &= \int_{\Omega} \mathbf{N}_{\sigma}^T \mathbf{C} \mathbf{N}_{\sigma} d\Omega, \quad \mathbf{B}^T = \int_{\Omega} \mathbf{B}_u^T \mathbf{N}_{\sigma} d\Omega, \\
\mathbf{D} &= \int_{\Omega} \mathbf{N}_r^T \frac{\Delta t^2}{\tilde{\rho}} \mathbf{N}_r d\Omega, \quad \mathbf{A}^T = \int_{\Omega} \mathbf{N}_u^T \mathbf{N}_r d\Omega, \\
\mathbf{M} &= \int_{\Omega} \mathbf{N}_{\sigma^e}^T \frac{\theta_3 \Delta t}{\eta} \mathbf{N}_{\sigma^e} d\Omega, \quad \mathbf{H} = \int_{\Omega} \mathbf{N}_k^T \frac{1}{\mathcal{H}_t} \mathbf{N}_k d\Omega, \\
\mathbf{f}^e &= \int_{\Omega} \mathbf{N}_u^T \tilde{\mathbf{b}} d\Omega + \int_{\Gamma_t} \mathbf{N}_u^T \tilde{\mathbf{t}} d\Gamma, \quad \mathbf{f}^c = \int_{\Omega} \mathbf{N}_{\sigma}^T \frac{\Delta t}{\eta} \boldsymbol{\sigma}_n^e d\Omega
\end{aligned} \tag{32}$$

243 The yield conditions are enforced at all Gauss integration points, with N_G being the total
244 number of such points. After solving the minimization part over Δu of program (31), and
245 transforming the maximum into a minimum with an opposite sign, we obtain

$$\begin{aligned}
& \min_{(\hat{\boldsymbol{\sigma}}, \hat{\boldsymbol{\tau}}, \hat{\boldsymbol{\sigma}}^e, \hat{\mathbf{r}}, \hat{\mathbf{k}})_{n+1}} \frac{1}{2} \Delta \hat{\boldsymbol{\sigma}}^T \mathbf{C} \Delta \hat{\boldsymbol{\sigma}} + \frac{1}{2} \hat{\mathbf{r}}_{n+1}^T \mathbf{D} \hat{\mathbf{r}}_{n+1} + \frac{1}{2} \Delta \hat{\boldsymbol{\sigma}}^{eT} \mathbf{M} \Delta \hat{\boldsymbol{\sigma}}^e \\
& + \frac{1}{2} \Delta \hat{\mathbf{k}}^T \mathbf{H} \Delta \hat{\mathbf{k}} + \Delta \hat{\boldsymbol{\sigma}}^{eT} \mathbf{f}^c \\
& \text{subject to } \mathbf{B}^T \hat{\boldsymbol{\sigma}}_{n+1} + \frac{1-\theta_1}{\theta_1} \mathbf{B}^T \hat{\boldsymbol{\sigma}}_n + \mathbf{A}^T \hat{\mathbf{r}}_{n+1} - \mathbf{f}^c = \mathbf{0} \\
& \Delta \hat{\boldsymbol{\sigma}}^e = \Delta \hat{\boldsymbol{\sigma}} - \Delta \hat{\boldsymbol{\tau}} \\
& F_j(\hat{\boldsymbol{\tau}}_{n+1}, \hat{\mathbf{k}}_{n+1}) \leq 0, \quad j=1, 2, \dots, N_G
\end{aligned} \tag{33}$$

247 The natural boundary condition (44) has been included through the terms \mathbf{f}^e , whereas the
248 imposition of essential boundary conditions for the displacements requires the introduction
249 of a new variable $\hat{\mathbf{r}}_{n+1}^u$ since the displacement increment $\Delta \mathbf{u}$ is a field variable for the dual

250 problem of program (33). More specifically, the program turns out to be

$$\begin{aligned}
& \min_{(\hat{\mathbf{g}}, \hat{\mathbf{t}}, \hat{\mathbf{g}}^e, \hat{\mathbf{r}}, \hat{\mathbf{k}}, \hat{\mathbf{r}}^u)_{n+1}} \frac{1}{2} \Delta \hat{\mathbf{g}}^T \mathbf{C} \Delta \hat{\mathbf{g}} + \frac{1}{2} \hat{\mathbf{r}}_{n+1}^T \mathbf{D} \hat{\mathbf{r}}_{n+1} + \frac{1}{2} \Delta \hat{\mathbf{g}}^{eT} \mathbf{M} \Delta \hat{\mathbf{g}}^e \\
& \quad + \frac{1}{2} \Delta \hat{\mathbf{k}}^T \mathbf{H} \Delta \hat{\mathbf{k}} + \Delta \hat{\mathbf{g}}^{eT} \mathbf{f}^c - \underline{(\mathbf{E} \mathbf{U}^d)^T \hat{\mathbf{r}}_{n+1}^u} \\
251 \quad \text{subject to} \quad & \mathbf{B}^T \hat{\mathbf{g}}_{n+1} + \mathbf{A}^T \hat{\mathbf{r}}_{n+1} - \underline{\mathbf{E} \hat{\mathbf{r}}_{n+1}^u} = \mathbf{f}^e - \frac{1-\theta_1}{\theta_1} \mathbf{B}^T \hat{\mathbf{g}}_n \quad (34) \\
& \Delta \hat{\mathbf{g}}^e = \Delta \hat{\mathbf{g}} - \Delta \hat{\mathbf{t}} \\
& F_j(\hat{\mathbf{t}}_{n+1}, \hat{\mathbf{k}}_{n+1}) \leq 0, \quad j=1, 2, \dots, N_G
\end{aligned}$$

252 where the essential boundary condition (44) are enforced, \mathbf{E} is an index matrix consisting of
253 entries equal to 0 and 1, \mathbf{U}^d is a vector consisting of the prescribed displacements at mesh
254 nodes, and the newly introduced $\hat{\mathbf{r}}_{n+1}^u$ represents the nodal reaction force. As shown, both the
255 objective function and the constraints of program (34) are altered (the underlined terms) due
256 to the imposition of the essential boundary conditions. The validity of the above can be
257 checked by differentiating the Lagrangian associated with the program (34) with respect to
258 $\hat{\mathbf{r}}_{n+1}^u$, resulting in

$$259 \quad \frac{\partial \mathcal{L}}{\partial \hat{\mathbf{r}}_{n+1}^u} = \mathbf{E} \mathbf{U}^d - \mathbf{E} \Delta \hat{\mathbf{u}}_{n+1} = \mathbf{0} \quad (35)$$

260 This is obviously the discretised form of the displacement boundary conditions (45).

261

262 Interaction between a deformable body and a rigid surface can be achieved in a
263 straightforward manner in the above program according to [35]. The classical Coulomb
264 model for frictional contact is adopted in this study, which is

$$265 \quad \begin{aligned}
& g_N \geq 0, \quad p \geq 0, \quad p g_N = 0, \\
& |q| - \mu p \leq 0
\end{aligned} \quad (36)$$

266 As shown in Figure 3, g_N is the gap between the material and the rigid surface, p is the

267 contact pressure which is positive corresponding to compression, q is the tangential stress,
 268 and μ is the friction coefficient between the material and the surface. After enforcing the
 269 conditions in (36) on finite element nodes, the principle reads

$$\begin{aligned}
 & \min_{(\hat{\boldsymbol{\sigma}}, \hat{\boldsymbol{\tau}}, \hat{\boldsymbol{\sigma}}^e, \hat{\mathbf{r}}, \hat{\mathbf{k}}, \hat{\mathbf{r}}^u)_{n+1}} \frac{1}{2} \Delta \hat{\boldsymbol{\sigma}}^T \mathbf{C} \Delta \hat{\boldsymbol{\sigma}} + \frac{1}{2} \hat{\mathbf{r}}_{n+1}^T \mathbf{D} \hat{\mathbf{r}}_{n+1} + \frac{1}{2} \Delta \hat{\boldsymbol{\sigma}}^e T \mathbf{M} \Delta \hat{\boldsymbol{\sigma}}^e \\
 & \quad + \frac{1}{2} \Delta \hat{\mathbf{k}}^T \mathbf{H} \Delta \hat{\mathbf{k}} + \Delta \hat{\boldsymbol{\sigma}}^e T \mathbf{f}^c - (\mathbf{E} \mathbf{U}^d)^T \hat{\mathbf{r}}_{n+1}^u + \sum_{j=1}^{n_c} g_{0j} p_j \\
 \text{subject to} \quad & \mathbf{B}^T \hat{\boldsymbol{\sigma}}_{n+1} + \mathbf{A}^T \hat{\mathbf{r}}_{n+1} - \mathbf{E} \hat{\mathbf{r}}_{n+1}^u + \mathbf{E}^c \boldsymbol{\rho} = \mathbf{f}^e - \frac{1-\theta_1}{\theta_1} \mathbf{B}^T \hat{\boldsymbol{\sigma}}_n \\
 270 \quad & \Delta \hat{\boldsymbol{\sigma}}^e = \Delta \hat{\boldsymbol{\sigma}} - \Delta \hat{\boldsymbol{\tau}} \tag{37} \\
 & p_k = -\mathbf{n}^T \boldsymbol{\rho}_k, \quad k = 1, \dots, n_c \\
 & q_k = -\hat{\mathbf{n}}^T \boldsymbol{\rho}_k, \quad |q_k| - \mu p_k \leq 0 \\
 & F_j^*(\hat{\boldsymbol{\tau}}_{n+1}, \hat{\mathbf{k}}_{n+1}) \leq 0, \quad j = 1, 2, \dots, N_G
 \end{aligned}$$

271 where $\boldsymbol{\rho} = (\rho_1, \rho_2)^T$ are the nodal forces, $\mathbf{n} = (n_1, n_2)^T$ and $\hat{\mathbf{n}} = (-n_2, n_1)^T$ are the normal and
 272 the tangent to the rigid boundary, \mathbf{E}^c is an index matrix of zeros and ones, and n_c is the
 273 number of potential contacts. The above program is the final optimization problem to be
 274 solved. While it may be solved in a number of ways using either general or specialized
 275 methods, it is transformed here into a second-order cone program (SOCP) and then resolved
 276 using the high performance optimization solver MOSEK [4]. The transformation of
 277 programs of the same type as (37) into a SOCP is straightforward, and has been
 278 documented in detail in [23, 34]. The main operation is to recast the quadratic terms in the
 279 objective function to linear ones, subject to a quadratic constraint, and to reform the yield
 280 function as a cone. Due to the attractive advantages presented in the introduction, a variety
 281 of mechanics problems have been formulated and solved in such a manner, including
 282 computational limit analysis of solids and plates [36-38], static/dynamic analysis of

283 elastoplastic frames and solids [21, 35, 39, 40], analysis of steady-state non-Newtonian
284 fluid flows [41], consolidation analysis [23], and the analysis of granular contact dynamics
285 [42-44].

286

287 5. Particle Finite Element Method

288 The Particle Finite Element Method (PFEM) is a Lagrangian approach capable of handling
289 general large deformation problems without any real limitation on the magnitude of the
290 deformation [27, 29, 45, 46]. Its major characteristic is to treat mesh nodes as ‘particles’ that
291 can move freely, and even separate from, the computational domain to which they originally
292 belong. The basic steps of the utilized PFEM are summarized (see also Figure 4) in the
293 following, with more details given in [35]:

- 294 (1) Suppose that we have a cloud of particles, C^n , at time t_n ;
- 295 (2) Identify the computational domain using the α -shape method [47] on the basis of C^n ;
- 296 (3) Create a finite element mesh, M^n , through a triangulation of the recognized domain
297 and discretize governing equations on M^n ;
- 298 (4) Map the state variables such as stresses, strains, velocities, etc. from the old mesh,
299 M^{n-1} , to the new mesh, M^n ;
- 300 (5) Solve the discrete governing equations on the new mesh, M^n , through a standard
301 finite element procedure;
- 302 (6) Update the position of mesh nodes to arrive at C^{n+1} and repeat.

303 To date, a number of challenging problems involving large deformation and free-surface
304 evolution have been tackled by the PFEM. These include the modelling of granular flows [24,
305 25, 35, 48, 49], landslides [29, 50], landslide-generated waves [30, 46], multi-fluid flows [51-
306 53], fluid-structure interaction [27, 54, 55], soil-structure interaction [35, 40], bubble

307 dynamics [56], the melting and spreading of polymers [57], industrial forming processes, and
308 the flow of fresh cement [58]. In this paper, the solution algorithm for elastoviscoplastic
309 analysis with strain softening is incorporated into the PFEM for progressive failure analysis
310 of sensitive clays. It is notable that the governing equations proposed are on the basis of the
311 infinitesimal strain theory which may lead to several errors for large deformation analysis.
312 The most serious one is the generation of strains as a result of rigid body motion. However, it
313 has been shown in [35, 59] that this and related errors are relatively minor when the time
314 steps used are small. As such, the price to pay for the convenience of being able to operate
315 with usual infinitesimal strain theory appears to be very small. Indeed, such a strategy has
316 been verified against analytical solutions for penetration problems [60] and validated
317 qualitatively as well as quantitatively against both quasi-static and dynamic collapse of a
318 granular column [24, 25] and the penetration of shallowly embedded pipelines [61].
319 Furthermore, it succeeds in reproducing a real-world flow-like landslide [29].

320

321 6. Numerical Examples

322 This section discusses numerical results for progressive failure analysis of sensitive clays
323 using the proposed approach. Note that finite element analysis of strain-softening materials
324 encounters issues of mesh sensitivity when using rate-independent models because the field
325 equations that describe the motion of the body may lose hyperbolicity. Indeed, the
326 corresponding boundary-value problem becomes ill-posed, with pathologically mesh-
327 dependent solutions in which the width of the shear bands depends on the mesh size. The
328 application of rate-dependent models is an effective way to circumvent this problem. It has
329 been shown that viscous terms introduce a length scale effect into the initial boundary-value
330 problem, even the rate-dependent model does not explicitly contain a parameter with the
331 dimension of length [62, 63]. Consequently, viscoplastic models result in solutions where the

332 shear bands have a finite width when strain localization occurs. It should be noted, however,
333 that the main objective of this work is to capture the entire failure process in sensitive clays
334 involving large deformation, rather than to predict the thickness of localized shear bands. As
335 noted by Moore [64], the typical thickness of a shear band in clay at failure is between 0.01
336 and 2 cm, and thus it is impractical to predict both the microscopic and macroscopic soil
337 response using a purely continuum model where a large earth structure is considered. One
338 possible way of accounting for the responses on both the macro and micro levels is through
339 the multiscale computational modelling technique [65-68].

340

341 6.1 One-dimensional elasto-viscoplastic problem

342 To verify the proposed variational principle, we consider an axial bar subject to a prescribed
343 load (Figure 5(a)). The material is represented by a one-dimensional elastoviscoplastic model
344 (Figure 5(b)). If the mass of the bar is sufficiently small, so that any induced inertial forces
345 are negligible, the load produces a uniform stress and strain along the bar and an analytical
346 solution is available. In the following, the material parameters of the bar are assumed to be:
347 Young's modulus $E = 5 \times 10^4$ Pa, the initial yield stress $\sigma_{Y_0} = 100$ Pa, and the viscosity
348 coefficient $\eta = 1000$ Pa·s.

349 The ability of the proposed formulation to capture the strain-rate dependence of the stress
350 response and stress relaxation behaviour is examined first. To this end, we set the prescribed
351 strain increase at a constant rate α until time $t^* = 0.4$ s and then hold the strain constant,
352 leading to stress relaxation. The analytical solution of this problem is available [69] and we
353 consider three different load rates, namely $\alpha = 0.2, 0.4,$ and 0.6 , respectively, to produce a
354 rate-dependent response (Figure 6(a)). The yield stress is set to be constant ($\sigma_Y = \sigma_{Y_0}$) in this
355 case (Figure 6(b)) and the time increment is $\Delta t = 2 \times 10^{-3}$ s in all simulations. Figure 7

356 illustrates the simulated stress response for different load rates as well as the corresponding
357 analytical solutions. For all cases, the resulting stresses increase in a stable manner until their
358 maximum values are reached. A higher load rate results in a larger maximum stress reflecting
359 the effect of viscosity. At the time $t=t^*$, the stresses for all three cases drop sharply
360 representing stress relaxation behaviour. Eventually, the residual stresses for all cases
361 asymptote towards the initial stress strength of the material, σ_{y_0} . All the simulated results
362 agree with the analytical solutions, which verifies the proposed variational formulation and
363 finite element implementation.

364

365 We now consider the details of strain-softening behaviour. The prescribed strain in this case
366 increases with a constant rate $\alpha=0.2$ (Figure 8(a)); however the yield stress strength σ_y ,
367 which equals $\sigma_{y_0}=100\text{Pa}$ at the beginning, reduces to its residual value $\sigma_{yR}=30\%\sigma_{y_0}$ when
368 the accumulated plastic strain reaches 7% (Figure 8(b)). Such a phenomenon of reduction has
369 been widely observed for materials undergoing plastic deformation. The initial and residual
370 yield stress strengths can be interpreted as strengths of a material at undisturbed and
371 remoulded states. The simulation is conducted using a total of 20, 30, and 40 time increments,
372 respectively, and again the agreement between the numerical and analytical solutions is
373 satisfactory (Figure 9).

374

375 6.2 Collapse of a sensitive clay column

376 As the second example, we consider the collapse of a sensitive clay column (Figure 10) in a
377 container which is 50 cm wide and 100 cm high. The container is lifted up quickly leading to
378 the spread of the sensitive clay. Such an experimental test has been widely used for
379 investigating the behaviour of granular matter [70-74], but has also been adopted for studying

380 the quickness of sensitive clays [1]. Here, the problem is considered to deform under plane-
381 strain conditions and only half of the geometry is modelled due to the symmetry. The
382 material parameters are as follows: Young's modulus $E = 5 \times 10^6$ Pa, Poisson's ratio $\nu = 0.49$,
383 density $\rho = 1.8 \times 10^3$ kg/m³, viscosity coefficient $\eta = 100$ Pa·s, undisturbed shear strength
384 $c_{up} = 5$ kPa, remoulded shear strength $c_{ur} = 1$ kPa, and $\bar{\kappa} = 25\%$. The frictional coefficient
385 between the clay and the rigid surface is taken as 0.3 and the gravitational acceleration
386 $g = -9.8$ m/s². The column is discretized using 7,962 6-node triangular elements with 16,199
387 nodes, and the time step utilized is $\Delta t = 0.01$ s.

388

389 The collapse procedure of the column obtained from the simulation is illustrated in Figure 11,
390 in which the colour is proportional to the accumulated equivalent plastic strain. The

391 normalized time \bar{t} refers to $\frac{t}{\sqrt{2h_0/g}}$ with h_0 being the initial height of the column. For

392 initially undisturbed sensitive clays, lifting the container results in two shear bands dividing

393 the column into three parts (Figure 11(a)). The upper part moves downward while the middle

394 part, which is in the shape of a triangle, is pushed out horizontally. After a considerable

395 movement of the middle part, a shear band is formed in the lower part (Figure 11(b)) and then

396 one more shear band appears in the upper part (Figure 11(c)). The second shear band in the

397 upper part deforms another layer of sensitive clay and the lower part, which was intact, is

398 disturbed significantly because of the shear band formed (Figure 11(d)). Further collapse of

399 the column leads to two more layers being squeezed out (Figure 11(e) and (f)). Localized

400 shear bands can be observed clearly in the final deposit, with some parts of the column

401 remaining undisturbed throughout the failure process. The collapse of remoulded sensitive

402 clay is also simulated for comparison (Figure 11). As shown, the collapse mechanism for this

403 case is quite different to the previous case of an undisturbed sample. Rather than fail

404 progressively, nearly all the material experiences plastic deformation with the material near
405 the bottom possessing the maximum equivalent plastic strain. Figure 12 shows the curves of
406 the front location and centre height against normalized time for columns of both initially
407 undisturbed and remoulded sensitive clays. The collapse of the column of remoulded clay
408 results in a final deposit with a much smaller height and considerably larger length. Both the
409 sensitive and remoulded clay columns reach their maximum run-out distance at around
410 $\bar{t} = 2.15$. However, the final centre height for the remoulded case is obtained earlier ($\bar{t} = 1.4$)
411 than that for the initially undisturbed case ($\bar{t} = 2.15$). Notably, the final centre height and
412 length are obtained simultaneously for the undisturbed sample, which differs from that for the
413 remoulded sample. The final mesh topology for both cases, illustrated in Figure 13, verifies
414 that the proposed approach can handle the extreme mesh distortion that accompanies failure
415 for this problem. A video of the collapse of both the remoulded and undisturbed sensitive
416 clay columns is provided in the supplementary materials.

417

418 To estimate the mesh sensitivity, the collapse of the initially undisturbed clay was also re-
419 analyzed using three different mesh sizes, where the length of the element edge was set to
420 $h = 1.0$ cm (1,934 triangles), 0.75 cm (3,528 triangles) and 0.5 cm (7,962 triangles). The
421 cases are referred to as coarse, medium, and fine meshes. As shown in Figure 14, the curves
422 of locations against time for all three tests agree well with each other. Moreover, all three
423 simulations result in very similar final deposits and shear bands (Figure 15), which proves
424 that a further decrease in the mesh size will not alter the form of the predicted failure mode.

425

426 6.3 Retrogressive collapse of a slope in sensitive clay

427 As observed in Scandinavia and eastern Canada, a fast and significant retrogressive collapse
428 of a slope in sensitive clay may be triggered by a small initial slide [2]. To illustrate the

429 ability of the proposed approach for modelling such a geohazard, we consider the sensitive
430 clay deposit shown in Figure 16. Here, collapse is triggered by removing a rigid triangular
431 block at the toe of the slope (which may be caused by erosion or excavation). The material
432 parameters of the sensitive clay are as follows: Young's modulus $E = 5 \times 10^6$ Pa, Poisson's
433 ratio $\nu = 0.33$, density $\rho = 1.8 \times 10^3$ kg/m³, viscosity coefficient $\eta = 100$ Pa·s, undisturbed
434 shear strength $c_{uu} = 22$ kPa, remoulded shear strength $c_{ur} = 1.2$ kPa, and $\bar{\kappa} = 25\%$. The
435 frictional coefficient between the sensitive clay and the rigid bottom surface is set to 0.1 and
436 the gravitational acceleration $g = -9.8$ m/s². A total of 18,420 6-noded triangular elements
437 (37,355 mesh nodes) is used to discretize the initial computational domain. The time step is
438 $\Delta t = 0.025$ s and the simulation proceeds until the final deposit is obtained.

439

440 The retrogressive failure process from the simulation is illustrated in Figure 17, with the
441 colour being proportional to the accumulated equivalent plastic strain. As illustrated, the
442 erosion leads to the first retrogressive collapse C1 in the slope (Figure 17(b)). Two shear
443 bands initiate from the bottom and propagate towards the top surface and the front inclined
444 surface, respectively, resulting in a graben. During the sliding, one more shear band is
445 generated in the graben dividing it into two elastic parts (Figure 17(c) and (d)). As the
446 disturbed mass due to collapse C1 moves far away from the new slip surface, the second
447 retrogressive collapse C2 occurs (Figure 17(e) and (f)). This mimics the first criterion for the
448 occurrence of retrogressive failure, that the slide debris should be able to flow out of the slide
449 area [1]. The same as that in C1, two plastic shear bands, also originating from the slope base,
450 are formed in C2 which results in a graben and a horst. The mass in front of the new slope
451 surface continues to move forward leading to the third retrogressive failure of the slope, C3
452 (Figure 17(g)). After this, a considerable amount of mass is deposited in front of the new
453 slope surface, resisting further collapse (Figure 17(h)). The final configuration of the slope,

454 shown in Figure 17(i), indicates that most of the clay involved in C2 and C3 has been
455 remoulded. This reflects the other criterion for the occurrence of retrogressive failure, which
456 states that the slide debris should be completely remoulded [1]. Eventually, the retrogressive
457 failure results in a deposit with a run-out distance of 28.71 m and a retrogression distance of
458 14.76 m (Figure 17(i)). A video of the entire failure process of the slope is available in the
459 supplementary materials.

460

461 The velocity of the sliding front and the maximum velocity were also recorded and are
462 depicted in Figure 18. As illustrated, the maximum velocity is not always located at the
463 sliding front. This can be explained by examining the velocity contour (Figure 19). The first
464 retrogressive failure results in the transformation of a part of the gravitational potential
465 energy of the mass into kinetic energy, with the remaining energy being dissipated by plastic
466 shearing (Figure 19(a)). The sliding front thus possesses the maximum velocity due to this
467 transformation. The second retrogressive collapse further releases potential gravitational
468 energy (Figure 19(b) and pushes the materials in front of it, consequently increasing the
469 velocity of the corresponding mass. In contrast, the velocity of the sliding front decreases
470 because of the friction along the basal surface and the effects of plastic dissipation. After a
471 while, the mass at the middle moves faster than the sliding front does as shown in Figure
472 19(c). The third retrogressive collapse further releases potential gravitational energy (Figure
473 19(d)). The velocity of the involved mass in collapse C3 is relatively low, however, because a
474 considerable body of clay with low velocity is located in front of the new slope surface. Note
475 that the sliding front already ceased at $t = 11.4$ s (Figure 19(e)). However, the clay at the
476 middle of the sliding mass continues to be pushed and moves forward, which eventually
477 disturbs the sliding front (Figure 19(f) and (g)).

478

479 The value of viscosity, back-calculated from various subaerial and submarine slides by
480 Edgers and Karlsrud [75] and Johnson and Rodine [76], is in the range of 100 to 1499 Pa·s .
481 We here investigate the effect of the viscosity on the retrogressive failure by analysing the
482 problem with varying viscosity coefficients of $\eta = 1 \text{ Pa}\cdot\text{s}$, $10 \text{ Pa}\cdot\text{s}$, $100 \text{ Pa}\cdot\text{s}$, and 1000
483 $\text{Pa}\cdot\text{s}$. Other material parameters for these simulations are the same as in the previous case.
484 As shown in Figure 20, retrogressive failure occurs four times for both $\eta = 1 \text{ Pa}\cdot\text{s}$ and 10
485 $\text{Pa}\cdot\text{s}$. Thus, the retrogression distances for these two cases, 20.25 m and 20.13 m, are very
486 close (Figure 21), although the run-out distance for $\eta = 1 \text{ Pa}\cdot\text{s}$ (38.18 m) is slightly larger
487 than that for $\eta = 10 \text{ Pa}\cdot\text{s}$ (36.73 m). When η is increased further, fewer retrogressive
488 failures are induced: for example three times for $\eta = 100 \text{ Pa}\cdot\text{s}$ and only twice for $\eta = 1000$
489 $\text{Pa}\cdot\text{s}$ (Figure 20). This means that an increase of η ($\eta > 10 \text{ Pa}\cdot\text{s}$) causes a decrease in the
490 run-out and retrogressive distance, as illustrated in Figure 21, because a higher viscosity
491 results in much more plastic dissipation and, consequently, less potential gravitational energy
492 is converted into kinetic energy. Such a decrease in energy transformation not only leads to a
493 smaller run-out distance, but also causes more clay to be deposited in front of the newly
494 formed slope surface which resists the occurrence of further retrogressive failure.

495

496 7. Conclusions

497 The progressive failure process of sensitive clays is simulated using the Particle Finite
498 Element Method with an advanced elastoviscoplastic model which is a combination of the
499 Bingham model (for describing rheological behaviour) and the Tresca model with strain-
500 softening (for capturing progressive failure behaviour). The resulting elastoviscoplastic
501 analysis is reformulated as an optimization problem on the basis of a mixed variational
502 principle and resolved in mathematical programming.

503

504 The proposed formulation is verified against the analytical solution of a one-dimensional
505 elastoviscoplastic problem. The capability of the proposed computational approach for
506 modelling progressive failure is illustrated by simulating the collapse of a column of sensitive
507 clay. Additionally, the retrogressive failure of a slope in sensitive clay is reproduced
508 successfully. The simulation results reflect the essential conditions for the occurrence of
509 retrogressive collapse which are that the slide debris should be fully remoulded and flow
510 away from the slide area. Furthermore, the effect of the viscosity of a sensitive clay on the
511 nature of retrogressive collapse is also studied. Numerical results show that an increase of
512 viscosity leads to a decrease in both the run-out distance and the retrogression distance due to
513 the dissipation of a large amount of energy.

514

515 Although the problem in this study is simulated under undrained conditions using total
516 stresses, an effective stress analysis can also be performed. This can be achieved by merging
517 the SOCP formulation for consolidation analysis of saturated porous media introduced in [23],
518 where rate-independent models are utilised, with the mixed variational principle presented in
519 this paper. The resulting formulation then can be incorporated into the particle finite element
520 method for investigating the hydro-mechanical mechanism in the progressive failure of
521 sensitive clays.

522

523 **Acknowledgements** The authors wish to acknowledge the support of the Australian Research
524 Council Centre of Excellence for Geotechnical Science and Engineering and the Australian
525 Research Council Discovery Project funding scheme (Project Number DP150104257).

526

527 **Appendix A.** Time discretization

528 The momentum conservation equation (1) is first discretized in time using the standard θ -
 529 method as:

$$530 \quad \nabla^T [\theta_1 \boldsymbol{\sigma}_{n+1} + (1 - \theta_1) \boldsymbol{\sigma}_n] + \mathbf{b} = \rho \frac{\mathbf{v}_{n+1} - \mathbf{v}_n}{\Delta t} \quad (38)$$

$$531 \quad \theta_2 \mathbf{v}_{n+1} + (1 - \theta_2) \mathbf{v}_n = \frac{\mathbf{u}_{n+1} - \mathbf{u}_n}{\Delta t} \quad (39)$$

532 where \mathbf{v} are velocities, θ_1 and θ_2 are parameters taking values in $[0, 1]$, the subscripts n and
 533 $n+1$ refer to the known and new, unknown states, and $\Delta t = t_{n+1} - t_n$ is the time step.

534 Rearranging the above equations leads to

$$535 \quad \nabla^T \boldsymbol{\sigma}_{n+1} + \frac{1 - \theta_1}{\theta_1} \nabla^T \boldsymbol{\sigma}_n + \tilde{\mathbf{b}} = \tilde{\rho} \frac{\Delta \mathbf{u}}{\Delta t^2} \quad (40)$$

$$536 \quad \mathbf{v}_{n+1} = \frac{1}{\theta_2} \left[\frac{\Delta \mathbf{u}}{\Delta t} - (1 - \theta_2) \mathbf{v}_n \right] \quad (41)$$

537 with the displacement increments $\Delta \mathbf{u} = \mathbf{u}_{n+1} - \mathbf{u}_n$ and

$$538 \quad \tilde{\rho} = \frac{\rho}{\theta_1 \theta_2} \quad (42)$$

$$539 \quad \tilde{\mathbf{b}} = \frac{1}{\theta_1} \mathbf{b} + \tilde{\rho} \frac{\mathbf{v}_n}{\Delta t} \quad (43)$$

540 The natural boundary condition is approximated in an analogous manner leading to

$$541 \quad \mathbf{N}^T (\boldsymbol{\sigma}_{n+1} + \frac{1 - \theta_1}{\theta_1} \boldsymbol{\sigma}_n) = \tilde{\mathbf{t}} \quad \text{on } \Gamma_t \quad \text{with } \tilde{\mathbf{t}} = \frac{1}{\theta_1} \bar{\mathbf{t}} \quad (44)$$

542 and the discretised essential boundary condition is

$$543 \quad \mathbf{u}_{n+1} = \bar{\mathbf{u}}_{n+1} \quad \text{on } \Gamma_u \quad (45)$$

544 By introducing another parameter $\theta_3 \in [0, 1]$, the incremental equations of the
 545 elastoviscoplastic model (Eqs. (6)-(10)) are

546
$$\Delta \boldsymbol{\varepsilon} = \Delta \boldsymbol{\varepsilon}^e + \Delta \boldsymbol{\varepsilon}^{vp} \quad (46)$$

547
$$\Delta \boldsymbol{\varepsilon}^e = \mathbb{C} \Delta \boldsymbol{\sigma} \quad (47)$$

548
$$(\boldsymbol{\sigma}_n + \theta_3 \Delta \boldsymbol{\sigma}) - (\boldsymbol{\tau}_n + \theta_3 \Delta \boldsymbol{\tau}) = \eta \frac{\Delta \boldsymbol{\varepsilon}^{vp}}{\Delta t} \Rightarrow (\Delta \boldsymbol{\sigma} - \Delta \boldsymbol{\tau}) + \frac{1}{\theta_3} (\boldsymbol{\sigma}_n - \boldsymbol{\tau}_n) = \frac{\eta}{\theta_3 \Delta t} \Delta \boldsymbol{\varepsilon}^{vp} \quad (48)$$

549
$$\Delta \boldsymbol{\varepsilon}^{vp} = \Delta \lambda \nabla_G F(\boldsymbol{\tau}_{n+1}) \quad (49)$$

550
$$F(\boldsymbol{\tau}_{n+1}) \leq 0; \Delta \lambda \geq 0; \Delta \lambda F(\boldsymbol{\tau}_{n+1}) = 0 \quad (50)$$

551 In summary, the governing equations for incremental analysis of elastoviscoplasticity consist
 552 of Eqs. (40), (41), (44)-(50).

553

554 **Reference**

- 555 1. Thakur, V. and Degago, S.A., Quickness of sensitive clays. *Géotechnique Letters*, 2012. **2**(3): p.
 556 87-95.
- 557 2. Locat, A., Leroueil, S., Bernander, S., Demers, D., Jostad, H.P., and Ouehb, L., Progressive
 558 failures in eastern Canadian and Scandinavian sensitive clays. *Canadian Geotechnical Journal*,
 559 2011. **48**(11): p. 1696-1712.
- 560 3. Jeong, S.W., Determining the viscosity and yield surface of marine sediments using modified
 561 Bingham models. *Geosciences Journal*, 2013. **17**(3): p. 241-247.
- 562 4. De Blasio, F.V., Elverhøi, A., Issler, D., Harbitz, C.B., Bryn, P., and Lien, R., Flow models of
 563 natural debris flows originating from overconsolidated clay materials. *Marine Geology*, 2004.
 564 **213**(1-4): p. 439-455.
- 565 5. Locat, J. and Demers, D., Viscosity, yield stress, remolded strength, and liquidity index
 566 relationships for sensitive clays. *Canadian Geotechnical Journal*, 1988. **25**(4): p. 799-806.
- 567 6. Quinn, P.E., Diederichs, M.S., Rowe, R.K., and Hutchinson, D.J., Development of progressive
 568 failure in sensitive clay slopes. *Canadian Geotechnical Journal*, 2012. **49**(7): p. 782-795.
- 569 7. Bernander, S., Kullingsjö, A., Gylland, A.S., Bengtsson, P.-E., Knutsson, S., Pusch, R., Olofsson,
 570 J., and Elfgren, L., Downhill progressive landslides in long natural slopes: triggering agents
 571 and landslide phases modeled with a finite difference method. *Canadian Geotechnical*
 572 *Journal*, 2016. **53**(10): p. 1565-1582.
- 573 8. Wang, B., Vardon, P.J., and Hicks, M.A., Investigation of retrogressive and progressive slope
 574 failure mechanisms using the material point method. *Computers and Geotechnics*, 2016. **78**:
 575 p. 88-98.
- 576 9. Dey, R., Hawlader, B., Phillips, R., and Soga, K., Large deformation finite-element modelling
 577 of progressive failure leading to spread in sensitive clay slopes. *Géotechnique*, 2015. **65**(8): p.
 578 657-668.
- 579 10. Dey, R., Hawlader, B.C., Phillips, R., and Soga, K., Numerical modelling of submarine
 580 landslides with sensitive clay layers. *Géotechnique*, 2016. **66**(6): p. 454-468.

- 581 11. Dey, R., Hawlader, B., Phillips, R., and Soga, K., Modeling of large-deformation behaviour of
582 marine sensitive clays and its application to submarine slope stability analysis. *Canadian*
583 *Geotechnical Journal*, 2016. **53**(7): p. 1138-1155.
- 584 12. Germanovich, L.N., Kim, S., and Puzrin, A.M., Dynamic growth of slip surfaces in catastrophic
585 landslides. *Proceedings of the Royal Society A: Mathematical, Physical and Engineering*
586 *Science*, 2016. **472**(2185).
- 587 13. Puzrin, A.M., Simple criteria for ploughing and runout in post-failure evolution of submarine
588 landslides. *Canadian Geotechnical Journal*, 2016. **53**(8): p. 1305-1314.
- 589 14. Viesca, R.C. and Rice, J.R., Nucleation of slip-weakening rupture instability in landslides by
590 localized increase of pore pressure. *Journal of Geophysical Research: Solid Earth*, 2012.
591 **117**(B3): p. n/a-n/a.
- 592 15. Palmer, A.C. and Rice, J.R., The Growth of Slip Surfaces in the Progressive Failure of Over-
593 Consolidated Clay. *Proceedings of the Royal Society of London. A. Mathematical and Physical*
594 *Sciences*, 1973. **332**(1591): p. 527-548.
- 595 16. Puzrin, A.M. and Germanovich, L.N., The growth of shear bands in the catastrophic failure of
596 soils. *Proceedings of the Royal Society A: Mathematical, Physical and Engineering Science*,
597 2005. **461**(2056): p. 1199-1228.
- 598 17. Puzrin, A.M., Germanovich, L.N., and Friedli, B., Shear band propagation analysis of
599 submarine slope stability. *Géotechnique*, 2016. **66**(3): p. 188-201.
- 600 18. Reissner, E., On a variational theorem in elasticity. *Journal of Mathematical Physics*, 1950. **24**:
601 p. 90-95.
- 602 19. Andersen, E.D., Roos, C., and Terlaky, T., On implementing a primal-dual interior-point
603 method for conic quadratic optimization. *Mathematical Programming*, 2003. **95**(2): p. 249-
604 277.
- 605 20. Sivaselvan, M.V., Complementarity framework for non-linear dynamic analysis of skeletal
606 structures with softening plastic hinges. *International Journal for Numerical Methods in*
607 *Engineering*, 2011. **86**(2): p. 182-223.
- 608 21. Krabbenhøft, K., Lyamin, A., and Sloan, S., Formulation and solution of some plasticity
609 problems as conic programs. *International Journal of Solids and Structures*, 2007. **44**(5): p.
610 1533-1549.
- 611 22. Makrodimitropoulos, A., Remarks on some properties of conic yield restrictions in limit analysis.
612 *International Journal for Numerical Methods in Biomedical Engineering*, 2010. **26**(11): p.
613 1449-1461.
- 614 23. Zhang, X., Sheng, D., Sloan, S.W., and Krabbenhoft, K., Second-order cone programming
615 formulation for consolidation analysis of saturated porous media. *Computational Mechanics*,
616 2016. **58**(1): p. 29-43.
- 617 24. Zhang, X., Ding, Y., Sheng, D., Sloan, S.W., and Huang, W., Quasi-static collapse of two-
618 dimensional granular columns: insight from continuum modelling. *Granular Matter*, 2016.
619 **18**(3): p. 1-14.
- 620 25. Zhang, X., Krabbenhoft, K., and Sheng, D., Particle finite element analysis of the granular
621 column collapse problem. *Granular Matter*, 2014. **16**(4): p. 609-619.
- 622 26. Zhang, X., Krabbenhoft, K., Pedrosa, D., Lyamin, A., Sheng, D., Da Silva, M.V., and Wang, D.,
623 Particle finite element analysis of large deformation and granular flow problems. *Computers*
624 *and Geotechnics*, 2013. **54**: p. 133-142.
- 625 27. Oñate, E., Celigueta, M.A., Idelsohn, S.R., Salazar, F., and Suárez, B., Possibilities of the
626 particle finite element method for fluid–soil–structure interaction problems. *Computational*
627 *Mechanics*, 2011. **48**(3): p. 307-318.
- 628 28. Cremonesi, M., Frangi, A., and Perego, U., A Lagrangian finite element approach for the
629 analysis of fluid-structure interaction problems. *International Journal for Numerical Methods*
630 *in Engineering*, 2010. **84**(5): p. 610-630.
- 631 29. Zhang, X., Krabbenhoft, K., Sheng, D., and Li, W., Numerical simulation of a flow-like

- 632 landslide using the particle finite element method. *Computational Mechanics*, 2015. **55**(1): p.
633 167-177.
- 634 30. Salazar, F., Irazábal, J., Larese, A., and Oñate, E., Numerical modelling of landslide-generated
635 waves with the particle finite element method (PFEM) and a non-Newtonian flow model.
636 *International Journal for Numerical and Analytical Methods in Geomechanics*, 2016. **40**(6): p.
637 809-826.
- 638 31. Potts, D.M., Dounias, G.T., and Vaughan, P.R., Finite element analysis of progressive failure
639 of Carsington embankment. *Géotechnique*, 1990. **40**(1): p. 79-101.
- 640 32. Troncone, A., Numerical analysis of a landslide in soils with strain-softening behaviour.
641 *Géotechnique*, 2005. **55**(8): p. 585-596.
- 642 33. Krabbenhoft, K., Lyamin, A.V., Sloan, S.W., and Wriggers, P., An interior-point algorithm for
643 elastoplasticity. *International Journal for Numerical Methods in Engineering*, 2007. **69**(3): p.
644 592-626.
- 645 34. Krabbenhoft, K. and Lyamin, A.V., Computational Cam clay plasticity using second-order
646 cone programming. *Computer Methods in Applied Mechanics and Engineering*, 2012. **209–**
647 **212**(0): p. 239-249.
- 648 35. Zhang, X., Krabbenhoft, K., Pedroso, D.M., Lyamin, A.V., Sheng, D., da Silva, M.V., and Wang,
649 D., Particle finite element analysis of large deformation and granular flow problems.
650 *Computers and Geotechnics*, 2013. **54**: p. 133-142.
- 651 36. Le, C.V., Nguyen-Xuan, H., and Nguyen-Dang, H., Upper and lower bound limit analysis of
652 plates using FEM and second-order cone programming. *Computers & Structures*, 2010. **88**(1–
653 2): p. 65-73.
- 654 37. Makrodimopoulos, A. and Martin, C.M., Upper bound limit analysis using simplex strain
655 elements and second-order cone programming. *International Journal for Numerical and*
656 *Analytical Methods in Geomechanics*, 2007. **31**(6): p. 835-865.
- 657 38. Makrodimopoulos, A. and Martin, C.M., Lower bound limit analysis of cohesive-frictional
658 materials using second-order cone programming. *International Journal for Numerical*
659 *Methods in Engineering*, 2006. **66**(4): p. 604-634.
- 660 39. Yonekura, K. and Kanno, Y., Second-order cone programming with warm start for
661 elastoplastic analysis with von Mises yield criterion. *Optimization and Engineering*, 2012.
662 **13**(2): p. 181-218.
- 663 40. Zhang, X., Sheng, D., Kouretzis, G.P., Krabbenhoft, K., and Sloan, S.W., Numerical
664 investigation of the cylinder movement in granular matter. *Physical Review E*, 2015. **91**(2): p.
665 022204.
- 666 41. Bleyer, J., Maillard, M., de Buhan, P., and Coussot, P., Efficient numerical computations of
667 yield stress fluid flows using second-order cone programming. *Computer Methods in Applied*
668 *Mechanics and Engineering*, 2015. **283**: p. 599-614.
- 669 42. Huang, J., da Silva, M.V., and Krabbenhoft, K., Three-dimensional granular contact dynamics
670 with rolling resistance. *Computers and Geotechnics*, 2013. **49**: p. 289-298.
- 671 43. Krabbenhoft, K., Huang, J., da Silva, M.V., and Lyamin, A.V., Granular contact dynamics with
672 particle elasticity. *Granular Matter*, 2012. **14**(5): p. 607-619.
- 673 44. Krabbenhoft, K., Lyamin, A.V., Huang, J., and Vicente da Silva, M., Granular contact dynamics
674 using mathematical programming methods. *Computers and Geotechnics*, 2012. **43**: p. 165-
675 176.
- 676 45. Oñate, E., Idelsohn, S.R., Del Pin, F., and Aubry, R., The Particle Finite Element Method - An
677 Overview. *International Journal of Computational Methods*, 2004. **01**(02): p. 267-307.
- 678 46. Cremonesi, M., Frangi, A., and Perego, U., A Lagrangian finite element approach for the
679 simulation of water-waves induced by landslides. *Computers & Structures*, 2011. **89**(11–12):
680 p. 1086-1093.
- 681 47. Edelsbrunner, H., M, E.P., #252, and cke, Three-dimensional alpha shapes. *ACM Trans.*
682 *Graph.*, 1994. **13**(1): p. 43-72.

- 683 48. Dávalos, C., Cante, J., Hernández, J.A., and Oliver, J., On the numerical modeling of granular
684 material flows via the Particle Finite Element Method (PFEM). *International Journal of Solids
685 and Structures*, 2015. **71**: p. 99-125.
- 686 49. Cante, J., Dávalos, C., Hernández, J.A., Oliver, J., Jonsén, P., Gustafsson, G., and Häggblad,
687 H.Å., PFEM-based modeling of industrial granular flows. *Computational Particle Mechanics*,
688 2014. **1**(1): p. 47-70.
- 689 50. Cremonesi, M., Ferri, F., and Perego, U., A basal slip model for Lagrangian finite element
690 simulations of 3D landslides. *International Journal for Numerical and Analytical Methods in
691 Geomechanics*, 2016: p. n/a-n/a.
- 692 51. Becker, P., Idelsohn, S.R., and Oñate, E., A unified monolithic approach for multi-fluid flows
693 and fluid–structure interaction using the Particle Finite Element Method with fixed mesh.
694 *Computational Mechanics*, 2015. **55**(6): p. 1091-1104.
- 695 52. Idelsohn, S.R., Mier-Torrecilla, M., Marti, J., and Oñate, E., *The Particle Finite Element
696 Method for Multi-Fluid Flows*, in *Particle-Based Methods: Fundamentals and Applications*, E.
697 Oñate and R. Owen, Editors. 2011, Springer Netherlands: Dordrecht. p. 135-158.
- 698 53. Idelsohn, S., Mier-Torrecilla, M., and Oñate, E., Multi-fluid flows with the Particle Finite
699 Element Method. *Computer Methods in Applied Mechanics and Engineering*, 2009. **198**(33–
700 36): p. 2750-2767.
- 701 54. Zhu, M. and Scott, M.H., Improved fractional step method for simulating fluid-structure
702 interaction using the PFEM. *International Journal for Numerical Methods in Engineering*,
703 2014. **99**(12): p. 925-944.
- 704 55. Cremonesi, M., Frangi, A., and Perego, U., A Lagrangian finite element approach for the
705 analysis of fluid–structure interaction problems. *International Journal for Numerical
706 Methods in Engineering*, 2010. **84**(5): p. 610-630.
- 707 56. Mier-Torrecilla, M., Idelsohn, S.R., and Oñate, E., Advances in the simulation of multi-fluid
708 flows with the particle finite element method. Application to bubble dynamics. *International
709 Journal for Numerical Methods in Fluids*, 2011. **67**(11): p. 1516-1539.
- 710 57. Oñate, E., Rossi, R., Idelsohn, S.R., and Butler, K.M., Melting and spread of polymers in fire
711 with the particle finite element method. *International Journal for Numerical Methods in
712 Engineering*, 2010. **81**(8): p. 1046-1072.
- 713 58. Cremonesi, M., Ferrara, L., Frangi, A., and Perego, U., Simulation of the flow of fresh cement
714 suspensions by a Lagrangian finite element approach. *Journal of Non-Newtonian Fluid
715 Mechanics*, 2010. **165**(23–24): p. 1555-1563.
- 716 59. Zhang, X., *Particle finite element method in geomechanics*, in *PhD Thesis*. 2014.
- 717 60. Hu, Y. and Randolph, M.F., A practical numerical approach for large deformation problems in
718 soil. *International Journal for Numerical and Analytical Methods in Geomechanics*, 1998.
719 **22**(5): p. 327-350.
- 720 61. Tian, Y., Cassidy, M.J., Randolph, M.F., Wang, D., and Gaudin, C., A simple implementation of
721 RITSS and its application in large deformation analysis. *Computers and Geotechnics*, 2014. **56**:
722 p. 160-167.
- 723 62. Needleman, A., Material rate dependence and mesh sensitivity in localization problems.
724 *Computer Methods in Applied Mechanics and Engineering*, 1988. **67**(1): p. 69-85.
- 725 63. Prevost, J.H. and Loret, B., Dynamic strain localization in elasto-(visco-)plastic solids, part 2.
726 plane strain examples. *Computer Methods in Applied Mechanics and Engineering*, 1990.
727 **83**(3): p. 275-294.
- 728 64. Moore, I.D. and Rowe, R.K., Numerical models for evaluating progressive failure in earth
729 structures—A review. *Computers and Geotechnics*, 1988. **6**(3): p. 217-239.
- 730 65. Andrade, J.E., Avila, C.F., Hall, S.A., Lenoir, N., and Viggiani, G., Multiscale modeling and
731 characterization of granular matter: From grain kinematics to continuum mechanics. *Journal
732 of the Mechanics and Physics of Solids*, 2011. **59**(2): p. 237-250.
- 733 66. Li, X., Zhang, X., and Zhang, J., A generalized Hill's lemma and micromechanically based

734 macroscopic constitutive model for heterogeneous granular materials. *Computer Methods in*
735 *Applied Mechanics and Engineering*, 2010. **199**(49–52): p. 3137-3152.

736 67. Guo, N. and Zhao, J., A coupled FEM/DEM approach for hierarchical multiscale modelling of
737 granular media. *International Journal for Numerical Methods in Engineering*, 2014. **99**(11): p.
738 789-818.

739 68. Li, X., Zhang, J., and Zhang, X., Micro-macro homogenization of gradient-enhanced Cosserat
740 media. *European Journal of Mechanics - A/Solids*, 2011. **30**(3): p. 362-372.

741 69. De Souza Neto, E.A., Peric, D., and Owen, D.R.J., *Computational Methods for Plasticity:*
742 *Theory and Applications*. 2008: John Wiley.

743 70. Lube, G., Huppert, H.E., Sparks, R.S.J., and Freundt, A., Collapses of two-dimensional
744 granular columns. *Physical Review E*, 2005. **72**(4).

745 71. Lajeunesse, E., Monnier, J.B., and Homsy, G.M., Granular slumping on a horizontal surface.
746 *Physics of Fluids*, 2005. **17**(10).

747 72. Balmforth, N.J. and Kerswell, R.R., Granular collapse in two dimensions. *Journal of Fluid*
748 *Mechanics*, 2005. **538**: p. 399-428.

749 73. Thompson, E.L. and Huppert, H.E., Granular column collapses: further experimental results.
750 *Journal of Fluid Mechanics*, 2007. **575**: p. 177-186.

751 74. Lacaze, L., Phillips, J.C., and Kerswell, R.R., Planar collapse of a granular column: Experiments
752 and discrete element simulations. *Physics of Fluids*, 2008. **20**(6).

753 75. Edgers, L. and Karlsrud, K., Soil flows generated by submarine slides - case studies and
754 consequences. *Norwegian Geotechnical Institute, Publication*, 1982(143): p. 1-10.

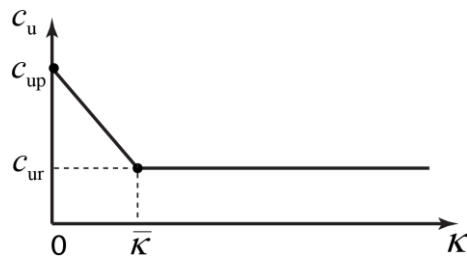
755 76. Johnson, A.M. and Rodine, J.R., *Debris flow*, in *Slope instability*, D. Brunsten and D.B. Prior,
756 Editors. 1984, Wiley: New York. p. 257-362.

757

758

759

760

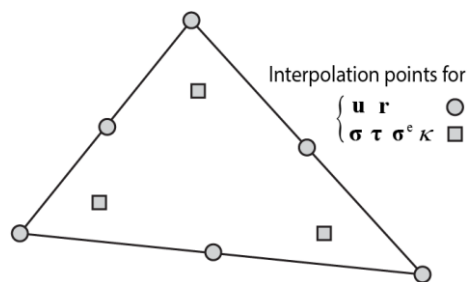


761

762 Figure 1. Variation of c_u with deviatoric plastic strain represented by parameter κ

763

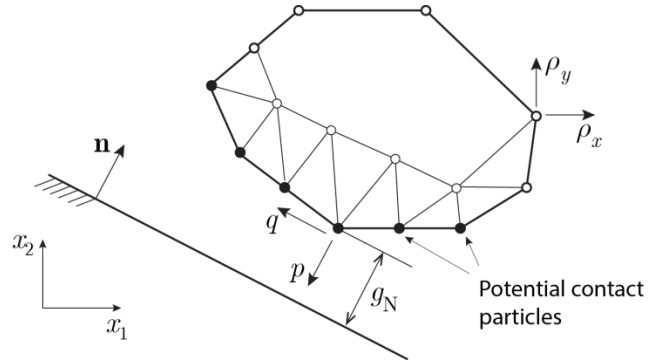
764



765

766
767
768
769
770
771
772

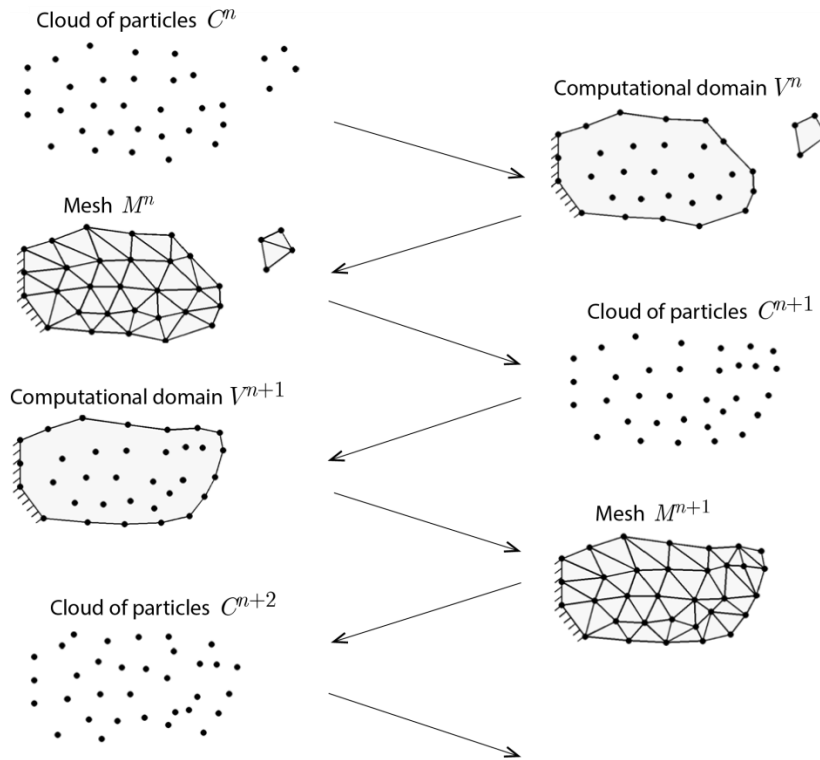
Figure 2. The mixed triangular element used in the simulation



773

774

Figure 3. The contact between a deformable body and a rigid surface

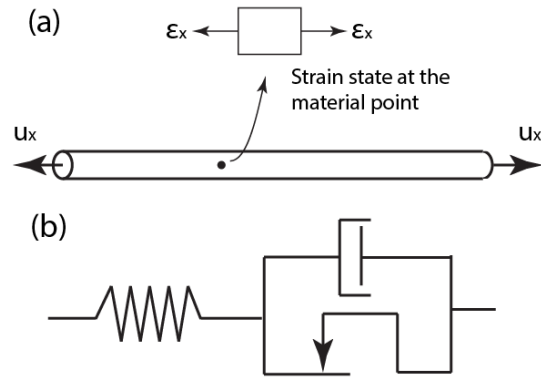


775

776

Figure 4. Steps for the Particle Finite Element Method (after [35])

777
778
779
780



781

782 Figure 5. (a) Schematic diagram of a bar subject to uniaxial loads; and (b) one-dimensional
 783 elastoviscoplastic model.

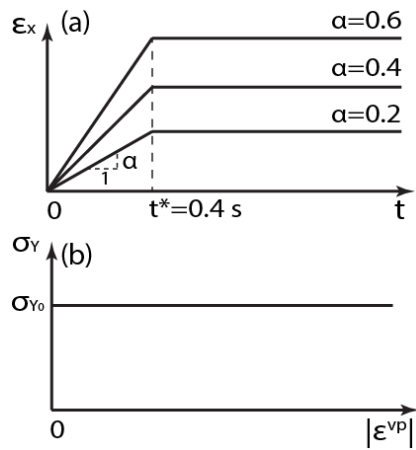
784

785

786

787

788



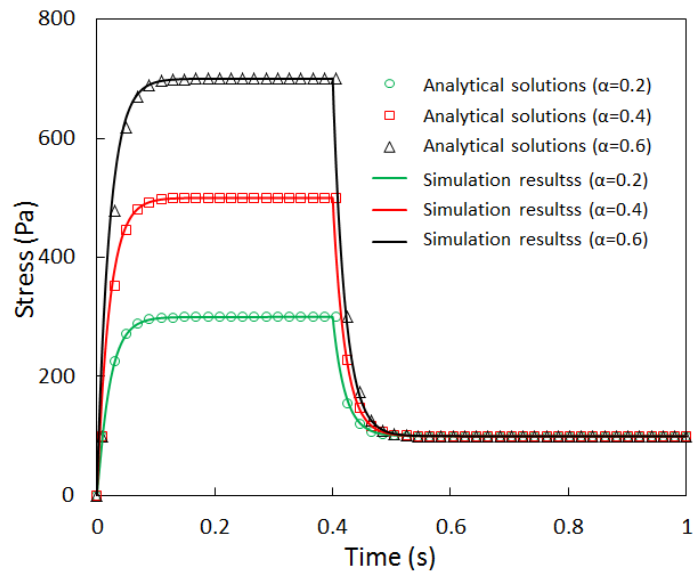
789

790 Figure 6. Curves of (a) the applied strain rate and (b) the variation of the yield stress for the
 791 one-dimensional stress relaxation problem

792

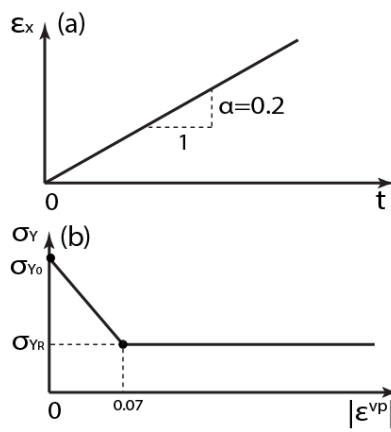
793

794



795

796 Figure 7. Comparison of numerical and analytical solutions for the one-dimensional stress
797 relaxation problem



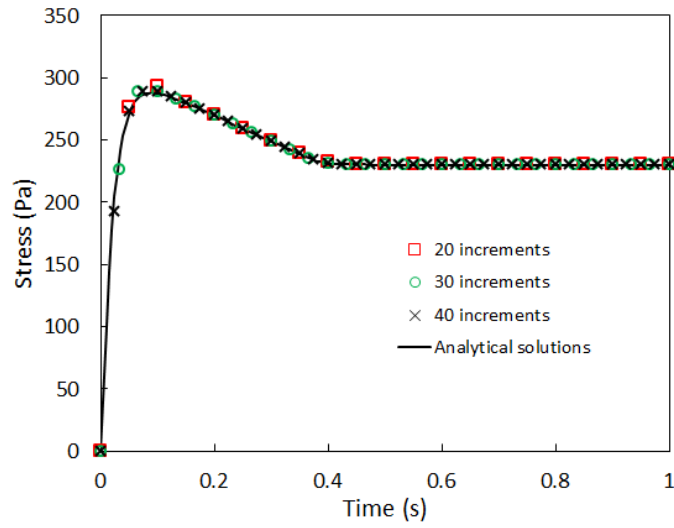
798

799 Figure 8. Curves of (a) the applied strain rate and (b) the variation of the yield stress for the
800 one-dimensional strain-softening problem

801

802

803

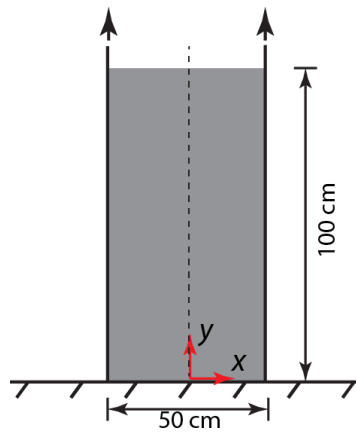


804

805 Figure 9. Comparison of numerical and analytical solutions for the one-dimensional
 806 elastoviscoplastic problem with strain softening

807

808

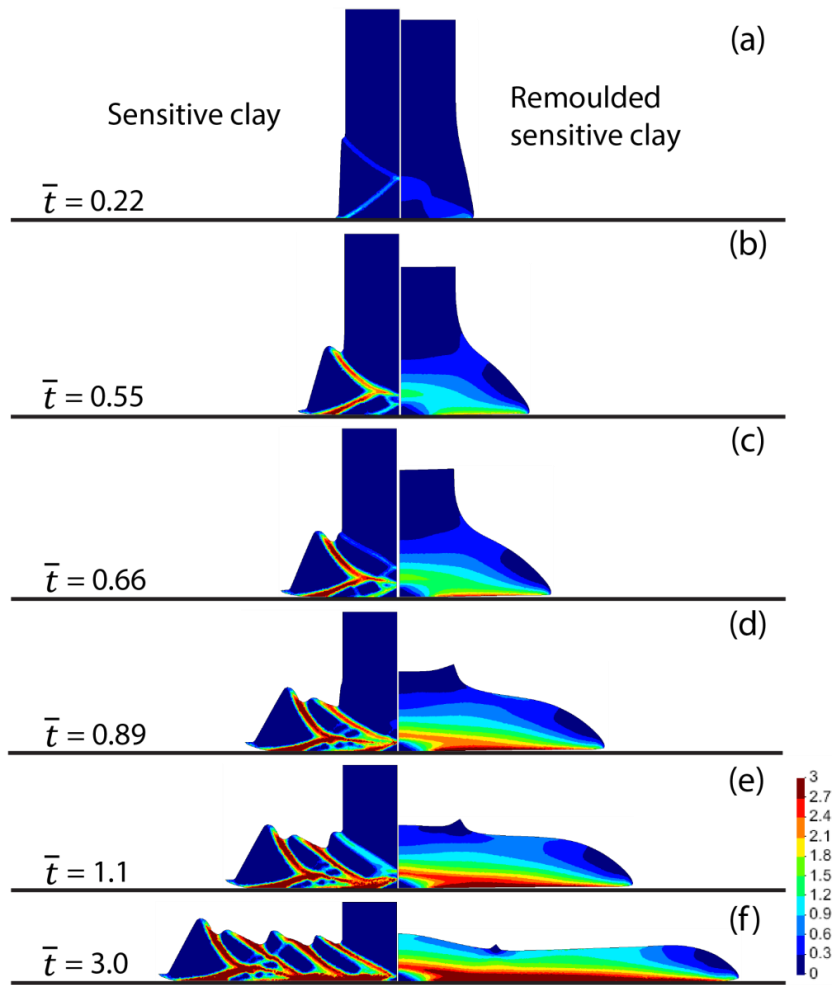


809

810 Figure 10. Schematic diagram for the collapse of a column of sensitive clays

811

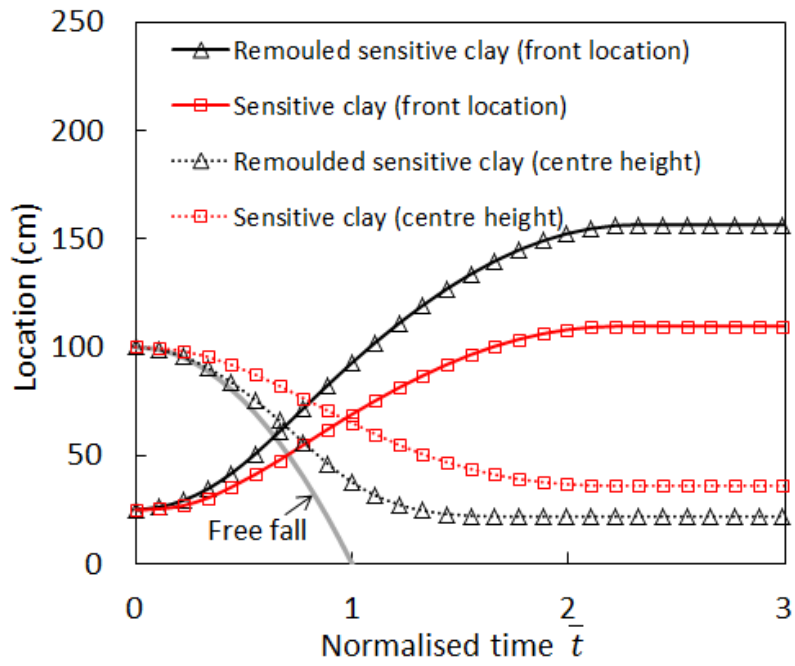
812



813

814 Figure 11. Collapse evolution processes of the column of initially undisturbed sensitive clays
 815 and remoulded sensitive clays. Colours are proportional to accumulated equivalent plastic
 816 strain

817



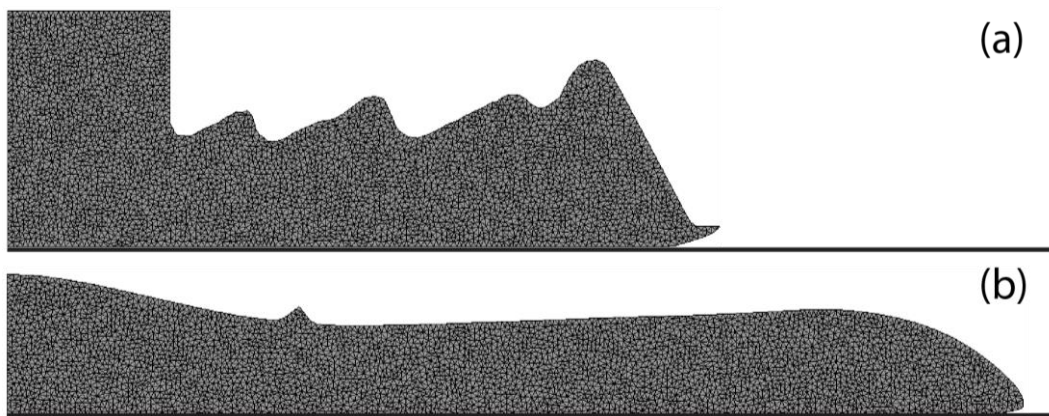
818

819 Figure 12. Curves of the front location and the centre height of the column against
820 normalized time

821

822

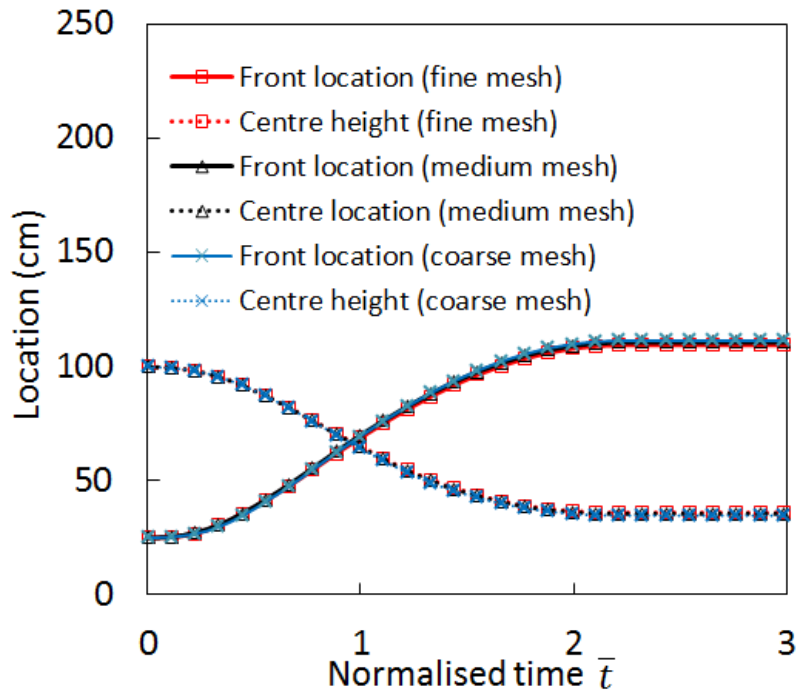
823



824

825

Figure 13. Final configuration with mesh topology illustrated



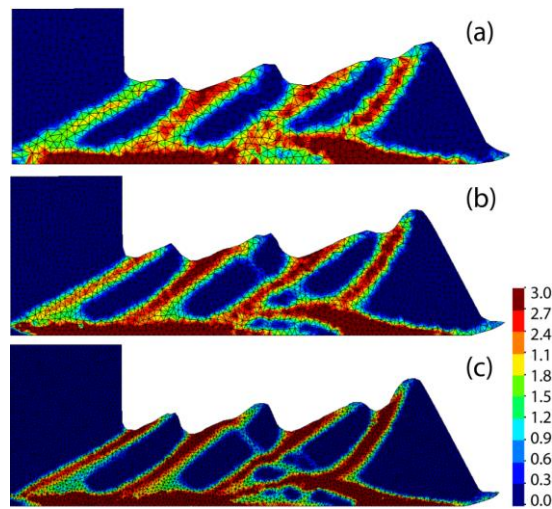
826

827 Figure 14. Effects of the utilized mesh size on the curves for front location and centre height
 828 of the column against normalized time

829

830

831



832

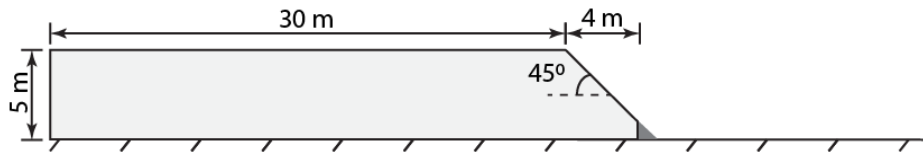
833 Figure 15. Final configurations and shear band distributions of the column collapse using (a)
 834 coarse meshes, (b) medium meshes, and (c) fine meshes. Colours are proportional to the
 835 accumulated equivalent plastic strain

836

837

838

839

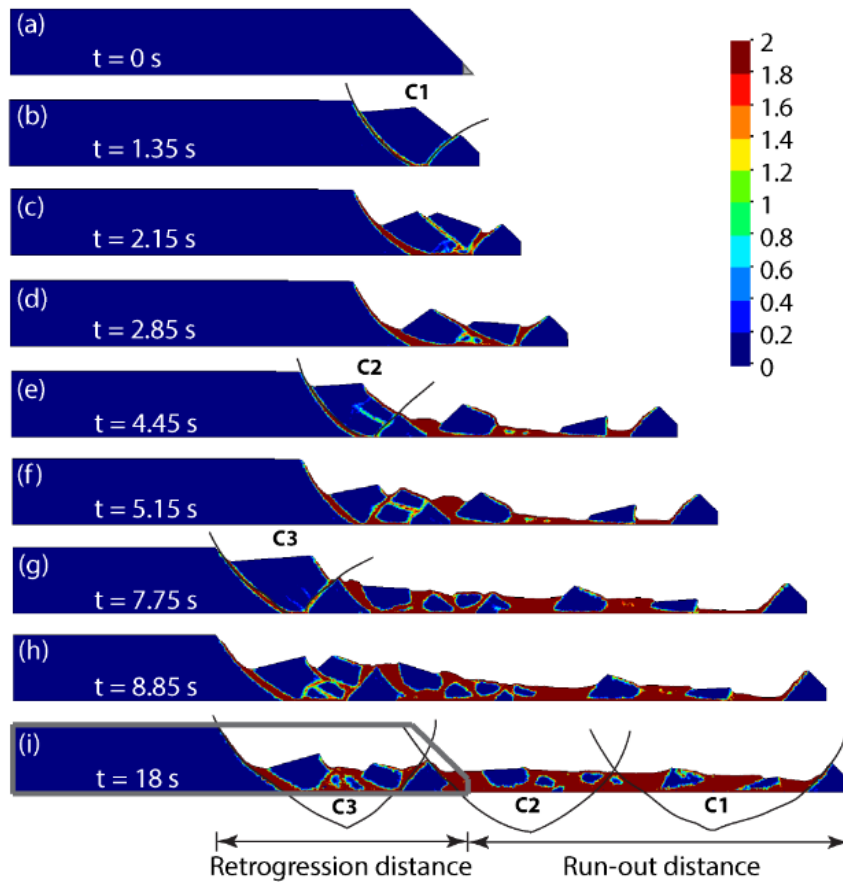


840

841 Figure 16. Schematic diagram for the retrogressive failure of a slope in sensitive clays.

842

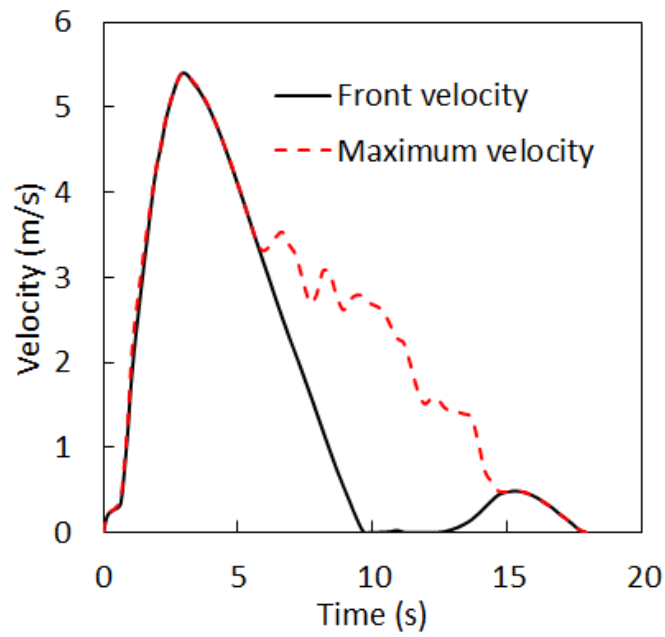
843



844

845 Figure 17. Retrogressive failure procedures of the slope. Colours are proportional to
846 accumulated equivalent plastic strain

847

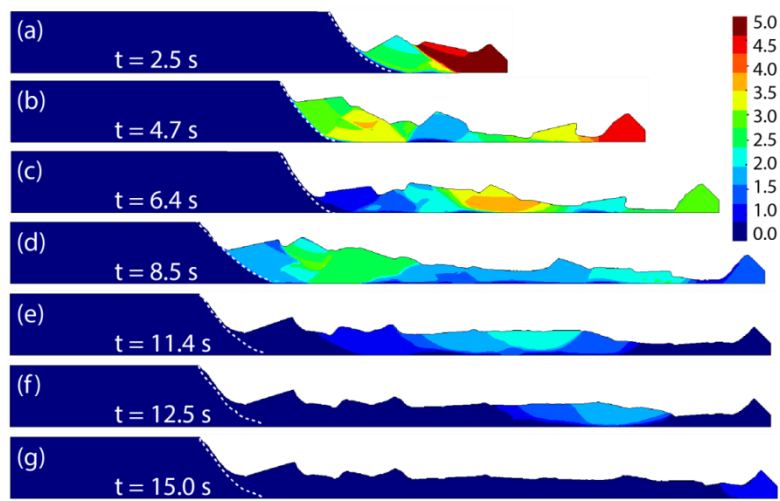


848

849 Figure 18. Velocity of the sliding front and the maximum velocity against time

850

851



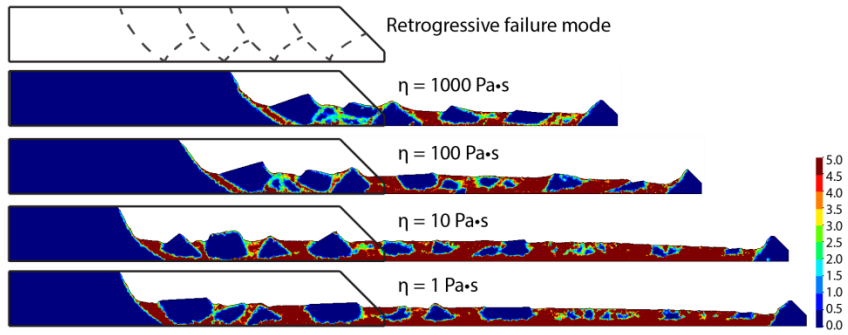
852

853 Figure 19. Velocity contour during the retrogressive failure

854

855

856



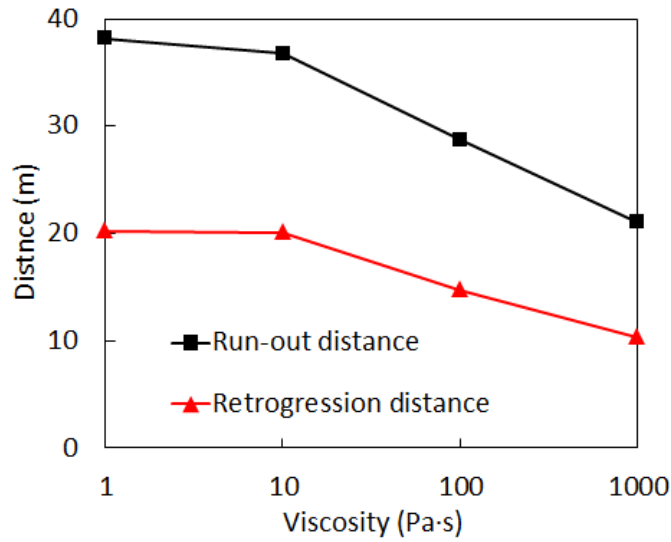
857

858 Figure 20. Final deposits from the simulation using different viscosity coefficients for
 859 sensitive clays

860

861

862



863

864 Figure 21. Curves of run-out distance and retrogression distance against viscosity